UNIVERSITATEA DIN BUCUREŞTI
Facultatea de Fizică
Şcoala Doctorală de Fizică

Irina-Nicoleta BRATOSIN

AN IN-DEPTH STUDY ON THE MECHANISMS BEHIND THE PHYSICAL PROPERTIES OF POROUS SILICON BASED SUPERCAPACITORS

PhD Thesis Summary

PhD Advisor
Prof. Dr. Daniela Dragoman

București, 2025

Content

Chapter 1

Preface

Whenever one starts studying electronic devices, there's a particular one which is more often than not ignored, and that is the power source, the ever-mysterious black box. The most attention it is given is when it is determined whether it is a current source or a potential source and whether it meets the requirements for the circuit it has to power. Rarely does it take the centre stage over the ever-needed transistor. Even in upgrading hardware, it is hardly given a thought whether the high demands of software would require a reasonably sized battery or not to power it.

This has recently changed, discussions taking more often place about whether batteries could potentially replace fossil fuels or AC generators, on which the present world is dependent, for perhaps a more sustainable approach to energy generation. Due to the possibility to generate and transmit it easier across long distances with minimal losses, AC generators took centre stage in energy generation, with DC power being limited only to portable devices with little power requirements. As technology inevitably kept advancing, more and more portable devices have emerged, with the added need of finding a portable power source that could last longer, be smaller, with a longer lifetime, more sustainable and affordable.

The demand for portable power led to the development of Li-ion batteries, and their limitations have since inspired innovations in supercapacitors. For a long time, Li-ion batteries dominated the portable power market, with supercapacitors remaining a less prominent alternative. However, as the drawbacks of Li-ion batteries start to outweigh their benefits, supercapacitors are now racing to catch up and perhaps even surpass them. With numerous advantages and significant potential for improvement, supercapacitors have been

the focus of much of my academic work. I have devoted considerable time to exploring how they could become a primary player in portable power as our world increasingly embraces mobility—from laptops and smartphones to tablets, smartwatches, and even cars. AC now feels more like a fuelling station for DC, supporting a society that values both portability and sustainability. As solar panels become more widespread, the need for advanced power storage will be crucial. With that in mind, I present my work on the development and improvement of silicon-based supercapacitor devices. While these supercapacitors aren't yet capable of powering a smartphone, they represent an important step toward that goal.

Will the stage belong once again to DC power, or will it again be left in the dark by what was once its superior substitute, the alternative current?

Chapter 2

Introduction

This work is based on Silicon electrodes modification towards building supercapacitors. Silicon was chosen as a base material since it is at the foundation of modern technology, which means that a Silicon based supercapacitor would be easier integrated in the existing technology. Silicon being an extensively studied material, as well as being compatible with a large variety of technological processes, it is a very appealing substrate for surface modifications. Coupling this with its behaviour as a reactive material it follows that electrodeposition is also a considerably feasible, cost-effective method for redox active compounds deposition. The supercapacitors in this work are based on a heavily doped porous-Si base, modified through multiple redox active compounds. The supercapacitor presented in Chapter 4, which had a thermally treated polymer deposited on it, exhibited a capacitance of around 8 F/cm^3. The following capacitor structure, on which Cobalt Hexacyanoferrate was further deposited, showed a capacitance of around 300 F/g, comparable to that of CNT-based capacitors. The subsequent one, in Chapter 6, on which a layer of TiN was further deposited, provided a capacitance of 75 F/g, but with a significant increase in stability compared to the other two structures.

The content of this thesis is structured by chapters as follows:

Chapter 3 will present a short description of the physical phenomena involved in charge storage and charge transfer inside a capacitor, as well as of the three main measurement methods used for assessing a supercapacitor's performance: Cyclic Voltammetry (CV), Electrochemical Impedance Spectroscopy (EIS) and Galvanostatic Charge Discharge (GCD).

Chapter 4 deals with electrical measurements of a porous Silicon supercapacitor on which a conductive polymer has been deposited and thermally treated towards becoming a carbon composite. This chapter will present how

electrical measurements were used to determine the degree of porosity and the length that optimize the charge storage performance.

Chapter 5 presents a continuation of the work in the previous chapter, involving the deposition on top of the structure of a cobalt hexacyanoferrate layer of nanocubes. Its performance is determined through electrical measurements, as well as via its ability to keep an LED on.

Chapter 6 deals with the subject of stability of a charge storage device. A TiN layer was deposited on top of the porous Silicon and carbon composite electrodes to form a supercapacitor which is able to withstand tens of thousands of charge-discharge cycles. Here electrical measurements are used in order to understand what the supercapacitor went through during the charging-discharging processes.

Chapter 7 introduces the programming language Julia in this work and presents how it is used for finding an equivalent circuit model for one of the types of supercapacitors described in Chapter 4. A parameter determination algorithm, which determines the corresponding circuit values from measured EIS data, is developed.

Chapter 8 presents three different methods which deal with problems encountered during the measuring process. The first one is an encapsulation system for encasing aqueous/gel electrolytes and preserving and protecting them from the surrounding environment towards ensuring measuring accuracy in prolonged measurements. The second method is employed to fabricate a contact on the back of the electrodes, in cases when a lateral one is not feasible. And the third method to enhance the performance of supercapacitors is a crocodile connector, which offers the possibility to fine tune the action of gripping a supercapacitor electrode.

Chapter 9 contains the conclusion of this thesis, where the work in this thesis is summarized, and my contributions and the impact of this work are presented.

Chapter 2 Bibliography

1. H. I. Becker, 'Low voltage electrolytic capacitor', US2800616A, Jul. 23, 1957 Accessed: Dec. 16, 2024. [Online]. Available: https://patents.google.com/patent/US2800616A/en
2. R. A. Rightmire, 'Electrical energy storage apparatus', US3288641A, Nov. 29, 1966 Accessed: Dec. 16, 2024. [Online]. Available: https://patents.google.com/patent/US3288641A/en
3. J. Phillips and H. Takei, 'Double layer capacitor', EP0120928A4, May 16, 1986 Accessed: Dec. 16, 2024. [Online]. Available: https://patents.google.com/patent/EP0120928A4/en
4. S. Trasatti and G. Buzzanca, 'Ruthenium dioxide: A new interesting electrode material. Solid state structure and electrochemical behaviour', *Journal of Electroanalytical Chemistry and Interfacial Electrochemistry*, vol. 29, no. 2, pp. A1–A5, Feb. 1971, doi: 10.1016/S0022-0728(71)80111-0.
5. H. Ji *et al.*, 'Capacitance of carbon-based electrical double-layer capacitors', *Nat Commun*, vol. 5, no. 1, p. 3317, Feb. 2014, doi: 10.1038/ncomms4317.
6. S. Ghosh *et al.*, 'Natural biomass derived hard carbon and activated carbons as electrochemical supercapacitor electrodes', *Sci Rep*, vol. 9, no. 1, p. 16315, Nov. 2019, doi: 10.1038/s41598-019-52006-x.
7. M. Sevilla and R. Mokaya, 'Energy storage applications of activated carbons: supercapacitors and hydrogen storage', *Energy Environ. Sci.*, vol. 7, no. 4, pp. 1250–1280, Mar. 2014, doi: 10.1039/C3EE43525C.

8. A. Ahmad *et al.*, ‘Preparation and Characterization of Physically Activated Carbon and Its Energetic Application for All-Solid-State Supercapacitors: A Case Study’, *ACS Omega*, vol. 8, no. 24, pp. 21653–21663, Jun. 2023, doi: 10.1021/acsomega.3c01065.
9. C. Liu, Z. Yu, D. Neff, A. Zhamu, and B. Z. Jang, ‘Graphene-Based Supercapacitor with an Ultrahigh Energy Density’, *Nano Lett.*, vol. 10, no. 12, pp. 4863–4868, Dec. 2010, doi: 10.1021/nl102661q.
10. B. Dharmasiri *et al.*, ‘Flexible carbon fiber based structural supercapacitor composites with solvate ionic liquid-epoxy solid electrolyte’, *Chemical Engineering Journal*, vol. 455, p. 140778, Jan. 2023, doi: 10.1016/j.cej.2022.140778.
11. L. F. Aval, M. Ghoranneviss, and G. B. Pour, ‘High-performance supercapacitors based on the carbon nanotubes, graphene and graphite nanoparticles electrodes’, *Heliyon*, vol. 4, no. 11, p. e00862, Nov. 2018, doi: 10.1016/j.heliyon.2018.e00862.
12. D. Majumdar, T. Maiyalagan, and Z. Jiang, ‘Recent Progress in Ruthenium Oxide-Based Composites for Supercapacitor Applications’, *ChemElectroChem*, vol. 6, no. 17, pp. 4343–4372, 2019, doi: 10.1002/celc.201900668.
13. A. K. Singh, D. Sarkar, K. Karmakar, K. Mandal, and G. G. Khan, ‘High-Performance Supercapacitor Electrode Based on Cobalt Oxide–Manganese Dioxide–Nickel Oxide Ternary 1D Hybrid Nanotubes’, *ACS Appl. Mater. Interfaces*, vol. 8, no. 32, pp. 20786–20792, Aug. 2016, doi: 10.1021/acsami.6b05933.
14. M. Alexandreli *et al.*, ‘Pseudocapacitive behaviour of iron oxides supported on carbon nanofibers as a composite electrode material for aqueous-based supercapacitors’, *Journal of Energy Storage*, vol. 42, p. 103052, Oct. 2021, doi: 10.1016/j.est.2021.103052.

15. W. Pholauyphon *et al.*, ‘Ultrahigh-performance titanium dioxide-based supercapacitors using sodium polyacrylate-derived carbon dots as simultaneous and synergistic electrode/electrolyte additives’, *Electrochimica Acta*, vol. 390, p. 138805, Sep. 2021, doi: 10.1016/j.electacta.2021.138805.
16. E. Sohouli, H. Teymourinia, A. Ramazani, and K. Adib, ‘Preparation of high-performance supercapacitor electrode with nanocomposite of CuO/NCNO flower-like’, *Sci Rep*, vol. 13, no. 1, p. 16221, Sep. 2023, doi: 10.1038/s41598-023-43430-1.
17. N. Maheswari and G. Muralidharan, ‘Controlled synthesis of nanostructured molybdenum oxide electrodes for high performance supercapacitor devices’, *Applied Surface Science*, vol. 416, pp. 461–469, Sep. 2017, doi: 10.1016/j.apsusc.2017.04.094.
18. A. Eftekhari, L. Li, and Y. Yang, ‘Polyaniline supercapacitors’, *Journal of Power Sources*, vol. 347, pp. 86–107, Apr. 2017, doi: 10.1016/j.jpowsour.2017.02.054.
19. M. Rajesh, C. J. Raj, R. Manikandan, B. C. Kim, S. Y. Park, and K. H. Yu, ‘A high performance PEDOT/PEDOT symmetric supercapacitor by facile in-situ hydrothermal polymerization of PEDOT nanostructures on flexible carbon fibre cloth electrodes’, *Materials Today Energy*, vol. 6, pp. 96–104, Dec. 2017, doi: 10.1016/j.mtener.2017.09.003.
20. K. Pandey and H. Kyung Jeong, ‘Silicon-Carbon nanofiber composite film for supercapacitor applications’, *Chemical Physics Letters*, vol. 834, p. 140972, Jan. 2024, doi: 10.1016/j.cplett.2023.140972.
21. C. Wang *et al.*, ‘Simple preparation of Si/CNTs/C composite derived from photovoltaic waste silicon powder as high-performance anode material for Li-ion batteries’, *Powder Technology*, vol. 408, p. 117744, Aug. 2022, doi: 10.1016/j.powtec.2022.117744.

22. A. Soam, K. Parida, R. Kumar, P. kavle, and R. O. Dusane, ‘Silicon-MnO2 core-shell nanowires as electrodes for micro-supercapacitor application’, *Ceramics International*, vol. 45, no. 15, pp. 18914–18923, Oct. 2019, doi: 10.1016/j.ceramint.2019.06.127.
23. S. Juyal *et al.*, ‘Development of integrated V2O5/mSi for supercapacitors: Exhibiting diffusion controlled charge storage dominance’, *Journal of Alloys and Compounds*, vol. 959, p. 170409, Oct. 2023, doi: 10.1016/j.jallcom.2023.170409.
24. Q. Zhou, Y. Zhou, M. Bao, and X. Ni, ‘Modified silicon nanowires@polypyrrole core-shell nanostructures by poly(3,4-ethylenedioxythiophene) for high performance on-chip micro-supercapacitors’, *Applied Surface Science*, vol. 487, pp. 236–243, Sep. 2019, doi: 10.1016/j.apsusc.2019.05.114.
25. W. Liu *et al.*, ‘High-performance supercapacitors based on free-standing SiC@PEDOT nanowires with robust cycling stability’, *Journal of Energy Chemistry*, vol. 66, pp. 30–37, Mar. 2022, doi: 10.1016/j.jechem.2021.07.007.

Chapter 3

Brief Presentation of Charge Storage Processes in a Supercapacitor and of the Electrical Measurement Methods Used

3.1 Description of the Electrochemical Double Layer

At the interface between an electrolyte, i.e., a liquid or gel containing ions, and a conductor submerged in it, charges building up at the surface of the conductor were observed. This phenomenon happens because, since charges are free to move in an electrolyte, some will be adsorbed on the surface of an electrode submerged in the liquid, and in return, charges of the opposite sign will develop on the said electrode surface, screening them. As a result, the two layers of charges form a charged capacitor, with capacitance values much larger than a classical capacitor since the distance between the layers is of the order of 10 nm (for a classic capacitor $C = \frac{\varepsilon S}{d}$).

When a conductive electrode is submerged in the electrolyte, the free electrons at the surface of the material will attract the positive ions in the electrolyte, building a barrier of charges.

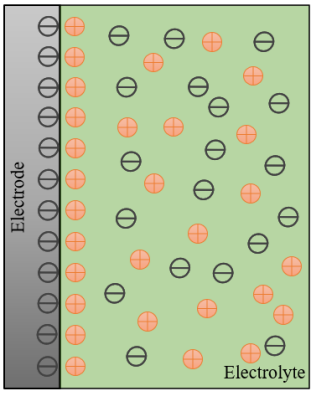

Figure 1. *Simplified diagram of the electrochemical double layer formation process*

3.2 The concept of Pseudocapacitance

One of the missing pieces for explaining the double layer was, for a while, the pseudocapacitance phenomenon. While charges building up at the surface (being adsorbed) involve mainly electrostatic interactions between charged specimens, the pseudocapacitance concept involves charge storage through redox reactions. Redox reactions refer to a chemical reaction between two elements/ compounds where one of them is oxidized and the other reduced. In the case of redox reactions, where electron transfer happens (as opposed to atom transfer), the oxidized part ceases an electron to the reduced part, which accepts the said electron. Then, the reduced element can also give the

electron back to the oxidized one, the reaction happening in reverse order. Due to this back-and-forth electron transfer and its storage to one element or the other, this could be seen and modelled as a capacitor charging or discharging, depending on the potential applied, similar to how a classical supercapacitor functions.

3.3 **Cyclic Voltammetry**

The main measurement method used for evaluating chemical reactions and their contributions to the total current is cyclic voltammetry (CV), which consists

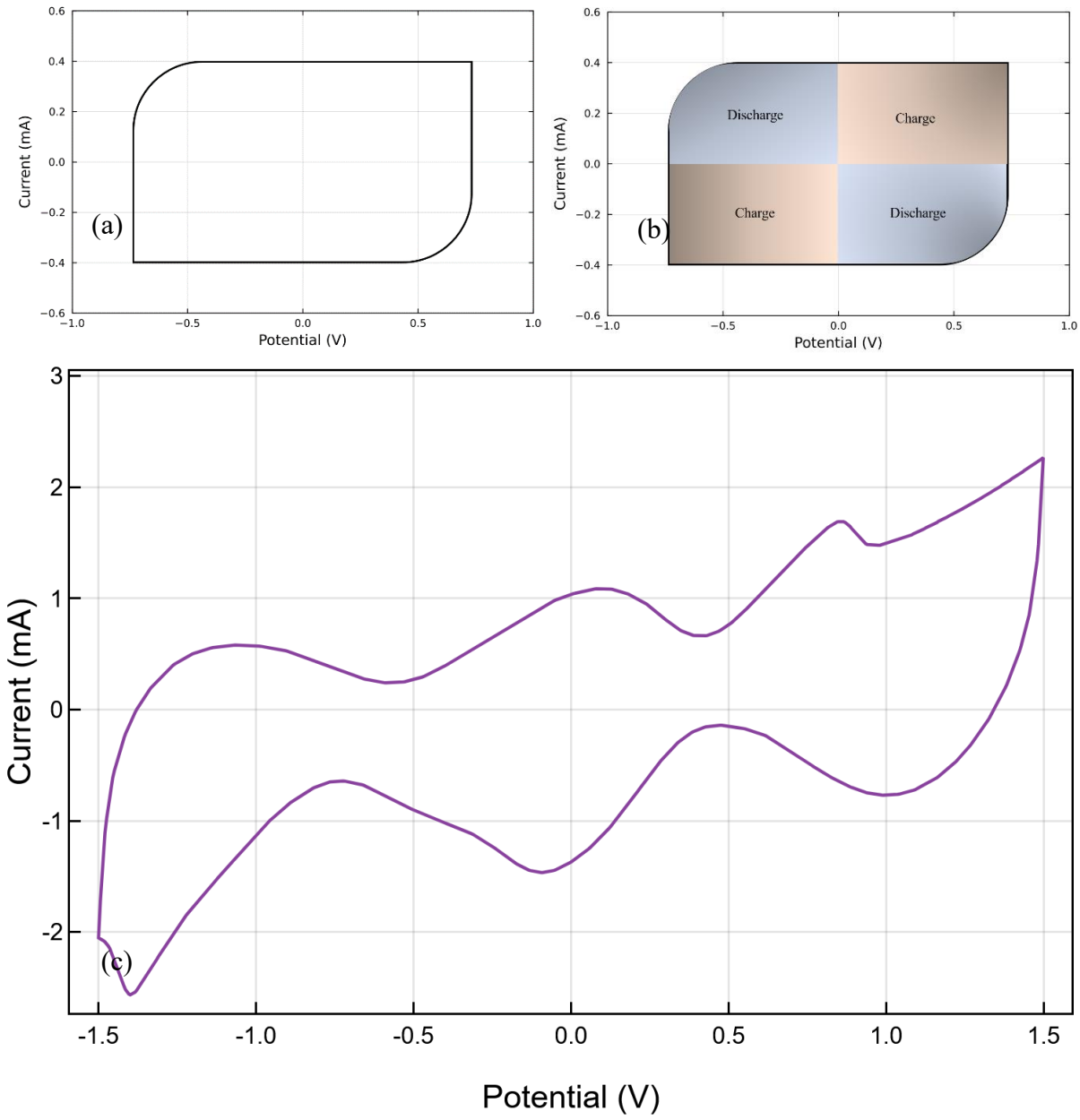

Figure 3. *(a) Idealized representation of CV curve for EDL. (b) Charge and discharge portions of the CV curve. (c) CV of a TiN electrode @ 500 mV/s*

of applying a triangular wave potential to the measured device. A triangular wave is applied because you need a function that is uniformly continuous, with a variable that is increasing linearly, and because in order to test redox reactions you need the potential to cycle back and forth through the same potential values. The measured physical property is the resulting current, plotted against the potential, basically an *I-V* characteristic, but returning through the same values as well. Figure 3(a) shows an idealized image of a CV (cyclic voltammogram) curve for a supercapacitor presenting double layer charge storage only.

In Figure 3(b), the charge and discharge regions of a CV curve when the potential increases from a negative to a positive value are represented. The sections are divided by quadrants. In the first quadrant, the potential goes from 0 to V_{max}, 0 being the reference potential. Since this is a charge storage device, when the potential increases, the device charges to the maximum value. Once it switches to the second quadrant, the potential decreases, going from V_{max} to 0, and the capacitor discharges. After crossing through 0, now to $-V_{max}$, the capacitor charges in the opposite direction, in the third quadrant, to discharge back to 0 V in the fourth quadrant. For the capacitance calculation, each quadrant is taken separately.

In the case of an ideal capacitor, the charging current remains constant, making the capacitance calculation straightforward. However, in a scenario such as the one in Figure 3(c), the redox reactions contribute to the total current, and their dependence on the potential complicates the behaviour of the super-capacitor, deviating it from the ideal capacitor behaviour.

3.4 **Electrochemical Impedance Spectroscopy**

While CV reveals information about the chemistry of the device, EIS (Electrochemical Impedance Spectroscopy) is a measurement method that reveals information about the electronic structure of the measured device, which aids in

finding an equivalent circuit that could further explain the physical processes taking place inside the capacitor.

The potential is defined as:

$$V = V_{max}\sin(\omega t)$$

(see Figure 4(a)). Using the Euler notation instead, $e^{j\varphi} = \cos\varphi + j\sin\varphi$, it becomes $V = V_m e^{j\omega t}$. Here j is used instead of i to not be confused with the electric current.

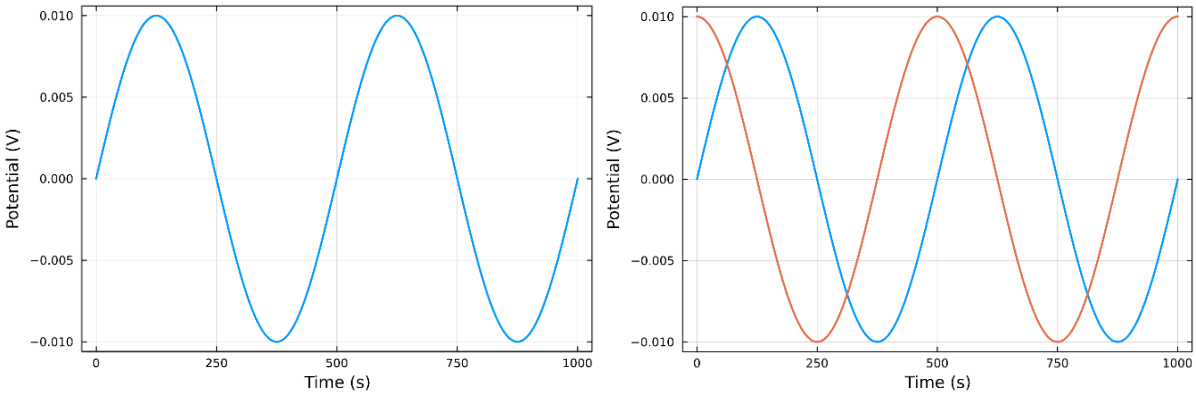

Figure 4. *(a) Potential signal. (b) Same signal plotted against the current signal*

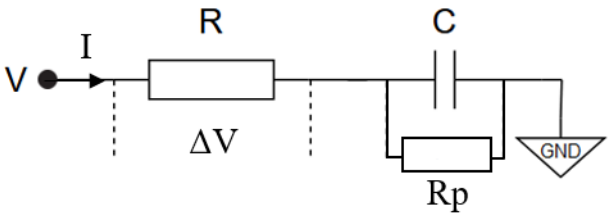

Figure 5. *A parallel RC circuit connected in series with a resistance*

When this potential is applied to a charge storage device, which obeys the relation $I = C\,\frac{dV}{dt}$, the current is written as:

$$I = C\,\frac{d}{dt}(V_m e^{j\omega t}) = j\omega C V_m e^{j\omega t}$$

From $I = j\omega CV \Rightarrow \frac{V}{I} = \frac{1}{j\omega C}$, which is the impedance of a capacitor, $Z_c = \frac{1}{j\omega C}$.

$$Z_l = Z(\cos\varphi + j\sin\varphi)$$

3.5 **Galvanostatic Charge Discharge**

Galvanostatic Charge Discharge (GCD) is the measurement that assesses just how good the tested supercapacitor is at storing charge. The measurement consists in a capacitor being charged at a constant current, so charging it at a constant rate, and plotting the measured potential against time. First, a positive current is applied, corresponding to the capacitor being charged, and then a negative current is applied, meaning the capacitor is being discharged. The theoretical potential vs time graph for a double layer capacitor looks as shown in Figure 8(a). This time, the reason why the dependence is a straight line in both directions is because the processes correspond to the reverse of what happens in CV. Now, a constant current means a constant derivative for the function $V(t)$, $I = C\ \frac{dV}{dt}$, I – constant, C – constant, so $\frac{dV}{dt}$ = constant, meaning a straight line, in each direction.

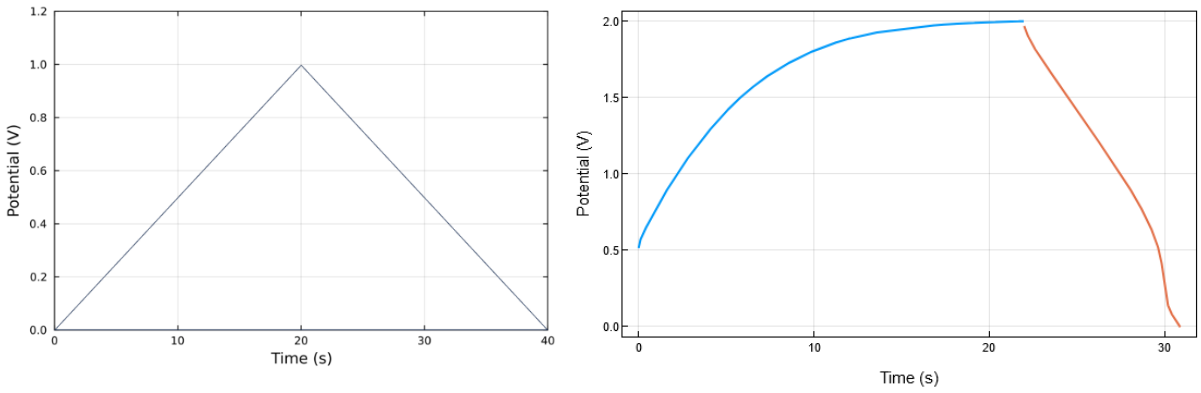

(a) (b)

Figure 8. *(a) Ideal Charge-Discharge graph for an EDL capacitor. (b) Charge-Discharge graph for a porous Si supercapacitor*

When reactions are involved, as seen from CV, the current becomes a potential-dependent function, and has no longer a constant value. When the potential value where a reaction takes place is reached, the current would either increase or decrease, depending if oxidation or reduction processes occur, while the source will still maintain the current value constant, therefore it will adjust

the potential accordingly, which will result in slope variations in $V(t)$. This is the GCD measurement (Figure 8(b)).

Chapter 3 Bibliography

1. R. Prasanna Misra, S. Das, and S. K. Mitra, 'Electric double layer force between charged surfaces: Effect of solvent polarization', *The Journal of Chemical Physics*, vol. 138, no. 11, p. 114703, Mar. 2013, doi: 10.1063/1.4794784.
2. S.-J. Park and M.-K. Seo, 'Chapter 1 - Intermolecular Force', in *Interface Science and Technology*, vol. 18, S.-J. Park and M.-K. Seo, Eds., in Interface Science and Composites, vol. 18., Elsevier, 2011, pp. 1–57. doi: 10.1016/B978-0-12-375049-5.00001-3.
3. A. H. B. Dourado, 'Electric Double Layer: The Good, the Bad, and the Beauty', *Electrochem*, vol. 3, no. 4, Art. no. 4, Dec. 2022, doi: 10.3390/electrochem3040052.
4. E. M. Purcell, *Electricity and Magnetism*. McGraw-Hill, 1985.
5. K. Doblhoff-Dier and M. T. M. Koper, 'Modeling the Gouy–Chapman Diffuse Capacitance with Attractive Ion–Surface Interaction', *J. Phys. Chem. C*, vol. 125, no. 30, pp. 16664–16673, Aug. 2021, doi: 10.1021/acs.jpcc.1c02381.
6. M. A. Brown, G. V. Bossa, and S. May, 'Emergence of a Stern Layer from the Incorporation of Hydration Interactions into the Gouy–Chapman Model of the Electrical Double Layer', *Langmuir*, vol. 31, no. 42, pp. 11477–11483, Oct. 2015, doi: 10.1021/acs.langmuir.5b02389.
7. M. A. Brown *et al.*, 'Determination of Surface Potential and Electrical Double-Layer Structure at the Aqueous Electrolyte-Nanoparticle Interface', *Phys. Rev. X*, vol. 6, no. 1, p. 011007, Jan. 2016, doi: 10.1103/PhysRevX.6.011007.

8. P. Bhojane, ‘Recent advances and fundamentals of Pseudocapacitors: Materials, mechanism, and its understanding’, *Journal of Energy Storage*, vol. 45, p. 103654, Jan. 2022, doi: 10.1016/j.est.2021.103654.
9. N. Elgrishi, K. J. Rountree, B. D. McCarthy, E. S. Rountree, T. T. Eisenhart, and J. L. Dempsey, ‘A Practical Beginner’s Guide to Cyclic Voltammetry’, *J. Chem. Educ.*, vol. 95, no. 2, pp. 197–206, Feb. 2018, doi: 10.1021/acs.jchemed.7b00361.
10. M. Rafiee, D. J. Abrams, L. Cardinale, Z. Goss, A. Romero-Arenas, and S. S. Stahl, ‘Cyclic voltammetry and chronoamperometry: mechanistic tools for organic electrosynthesis’, *Chem. Soc. Rev.*, vol. 53, no. 2, pp. 566–585, Jan. 2024, doi: 10.1039/D2CS00706A.
11. Lämmel C., Schneider M., Weiser M., Michaelis A. Investigations of electrochemical double layer capacitor (EDLC) materials - a comparison of test methods // Materialwissenschaft und Werkstofftechnik. 2013
12. Alexandros Ch. Lazanas and Mamas I. Prodromidis, Electrochemical Impedance Spectroscopy─A Tutorial, ACS Measurement Science Au 2023 3 (3)
13. M. E. Orazem and B. Tribollet, *Electrochemical Impedance Spectroscopy*. John Wiley & Sons, 2011.
14. A. Lasia, Electrochemical Impedance Spectroscopy and its Applications, book, Springer, 2014
15. L. E. Helseth, ‘The nonlinearities in the galvanostatic charging curves of supercapacitors provide insights into charging mechanisms’, *Journal of Energy Storage*, vol. 55, p. 105440, Nov. 2022, doi: 10.1016/j.est.2022.105440.

Chapter 4

Porous Si-based Supercapacitors and the Determination of the Effects of Porosity on their Performance

In the first part of this chapter, the work done on improving porous Silicon capacitors through polymerization and thermal treatment will be presented. Two different parameters in the fabrication process were varied and used for comparison between samples, namely the current density and the exposure time, and from electrical measurements an explanation for the physical processes present was developed. The main goal of the work in this chapter was to determine which parameter values in the porosity-inducing process would yield the best results in terms of capacitance value, energy density, stability and redox contribution.

4.1 **Fabrication of Porous Silicon Electrodes**

The fabrication process involved the treatment of silicon wafers (provided by Siegert Wafer GmbH), which were boron-doped with a resistivity of 1−5 mΩ cm and had a (100) crystallographic orientation, by electrochemical etching in a 1:1 (v/v) electrolyte solution (40 wt% HF and 98 wt% ethanol) at constant current densities ranging from 10 to 110 mA/cm^2. This anodization process was conducted for two different durations, namely, 5 and 10 minutes, resulting in the creation of 12 distinct types of electrodes with varying degrees of porosity. Before the electrodes underwent polymerization, the native oxide layer was eliminated by immersing them in a 5% (v/v) aqueous HF solution for 3 minutes, followed by rinsing with deionized water and drying under N_2. The electrochemical deposition of 7-hydroxy-1,2,3,4-tetrahydro-naphthalene-2-carboxylic acid onto the silicon electrode through potentiometry was performed using an Autolab

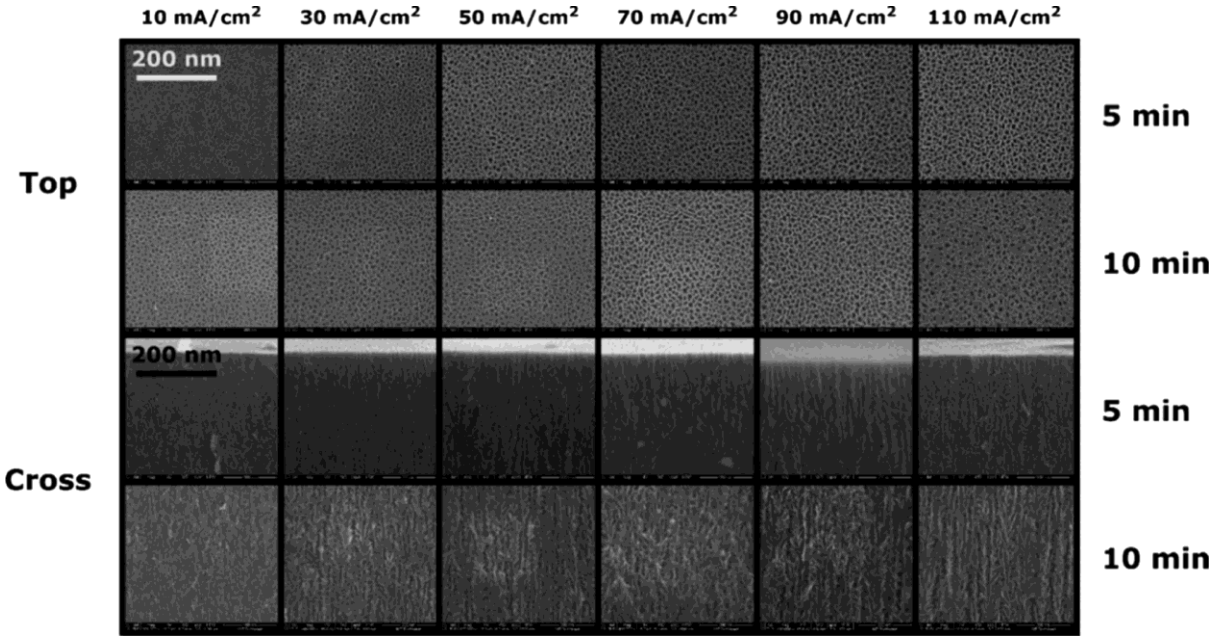

Figure 1. *SEM images for each porous electrode obtained, top & cross* sections

302N apparatus equipped with FRA 32 M, SCAN 250, and ADC 10 M modules, applying a constant current density of 39 mA/cm^2 for 120 seconds in a solution containing 2 mM 7-hydroxy-1,2,3,4-tetrahydronaphthalene-2-carboxylic acid in 10 mM PBS and 0.1 M KCl as the electrolyte. The electrodeposition step was also performed to passivate the Silicon layer, since it is well known that Silicon is quite reactive with many electrolytes [1,2]. The porous silicon sample served as the working electrode, a saturated calomel electrode acted as the reference electrode, and a Pt wire functioned as the counter electrode.

4.2 **Evaluation of Supercapacitors' Performance Through Cyclic Voltammetry**

Initially, cyclic voltammetry (CV) measurements were conducted on each symmetric plane parallel supercapacitor assembled and the voltammograms obtained at a scan rate of 50 mV/s were compared.

Figures 3(a) and (b) display the profiles obtained from each electrode after 5 and 10 minutes, respectively. Upon examining the current values of each electrode, we can preliminarily observe that for the 5-minute duration, the

electrode treated at 70 mA/cm^2 exhibits the highest current value, whereas for the 10-minute duration, it is the electrode processed at 110 mA/cm^2 which showed the highest current.

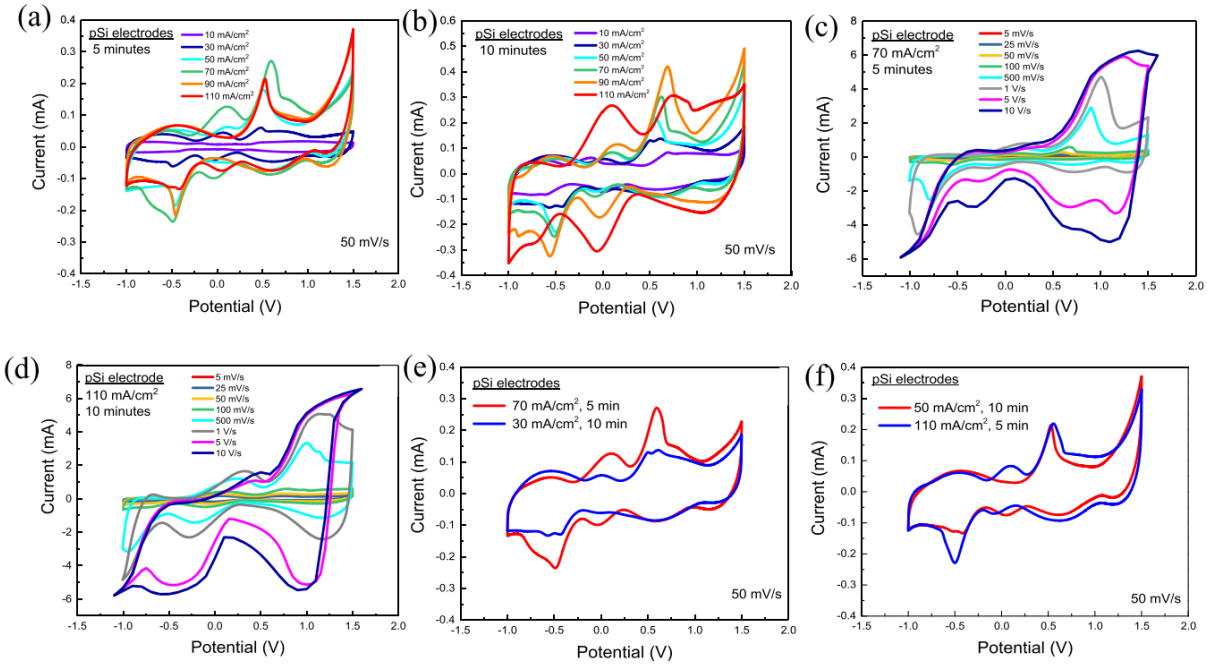

Figure 3. *CV profiles for the supercapacitor with electrodes obtained at 70 mA/cm^2 for 5 min (a) and 110 mA/cm^2 at 10 min (b); comparison between voltammograms recorded at 50 mV/s for 5 min (c), respectively, and 10 min (d); comparison between two electrodes obtained at the same porosity (e) and same pore length (f)*

Although the redox peaks indicate a greater deposition of polymer at 110 mA/cm^2, based on the voltammetry curves exhibiting a larger current value reached at the same or similar potential values, they appear less distinct compared to those at 90 mA/cm^2 or even its 5-minute counterpart. Upon closer examination of the behavior of electrodes treated at 70 mA/cm^2 for 5 minutes and those at 110 mA/cm^2 for 10 minutes, we analyze the recorded CV profiles across scan rates ranging from 5 mV/s to 10 V/s (Figure 3(c) and (d)).

To provide a quantitative explanation, the capacitance has been determined from the discharging regions of the voltammograms of each capacitor. These discharging regions occur in the second and fourth quadrants, where the potential across the capacitor decreases from its chosen maximum value, either -1 or 1.5

V, depending on the current direction. First the absolute capacitance, C_{abs}, was calculated using the formula presented in the previous chapter and plotted against the scan rate in Figures 4(a) and 4(b) for each current density, and separated by the exposure time. Then, the obtained capacitance for each supercapacitor was divided by the porous volume given in Table 1(d), to obtain the volumetric capacitance, C_v, which was plotted in a similar manner as the absolute value in Figures 4(c) and 4(d). The reason why the volumetric capacitance was chosen was because most of the exposed area is inside the electrode, the porosity process producing channels inside the silicon that would be filled by the electrolyte, therefore making the volumetric capacitance more relevant than the surface capacitance.

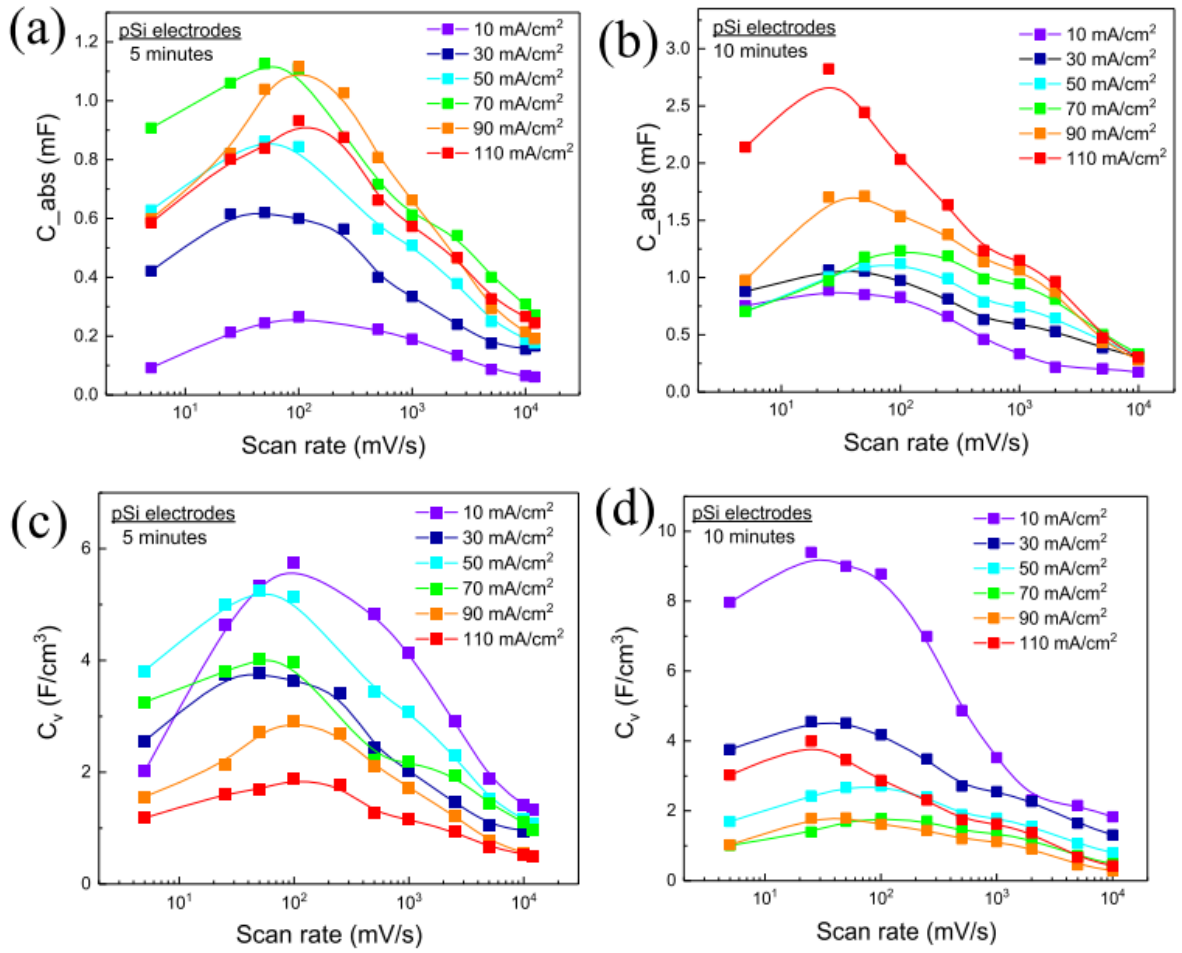

Figure 4. *Capacitance vs scan rate for symmetric supercapacitors assembled using electrodes porosified 5 (a) and 10 min (b), respectively; (c,d) corresponding volumetric capacitances vs scan rates.*

4.3 **Galvanostatic Charge Discharge Measurements**

Galvanostatic charge-discharge (GCD) measurements were conducted by applying a constant current and monitoring the potential evolution across each device. The potential range selected extended from 0 to 1.4 V on the positive side and from 0 to -1 V on the negative side. The decision to set the upper limit at 1.4 V instead of 1.5 V was motivated by concerns regarding electrode oxidation at higher voltage rates, which could compromise the device's longevity, especially at high currents [14]. Current values ranged from 100 µA to 1 mA.

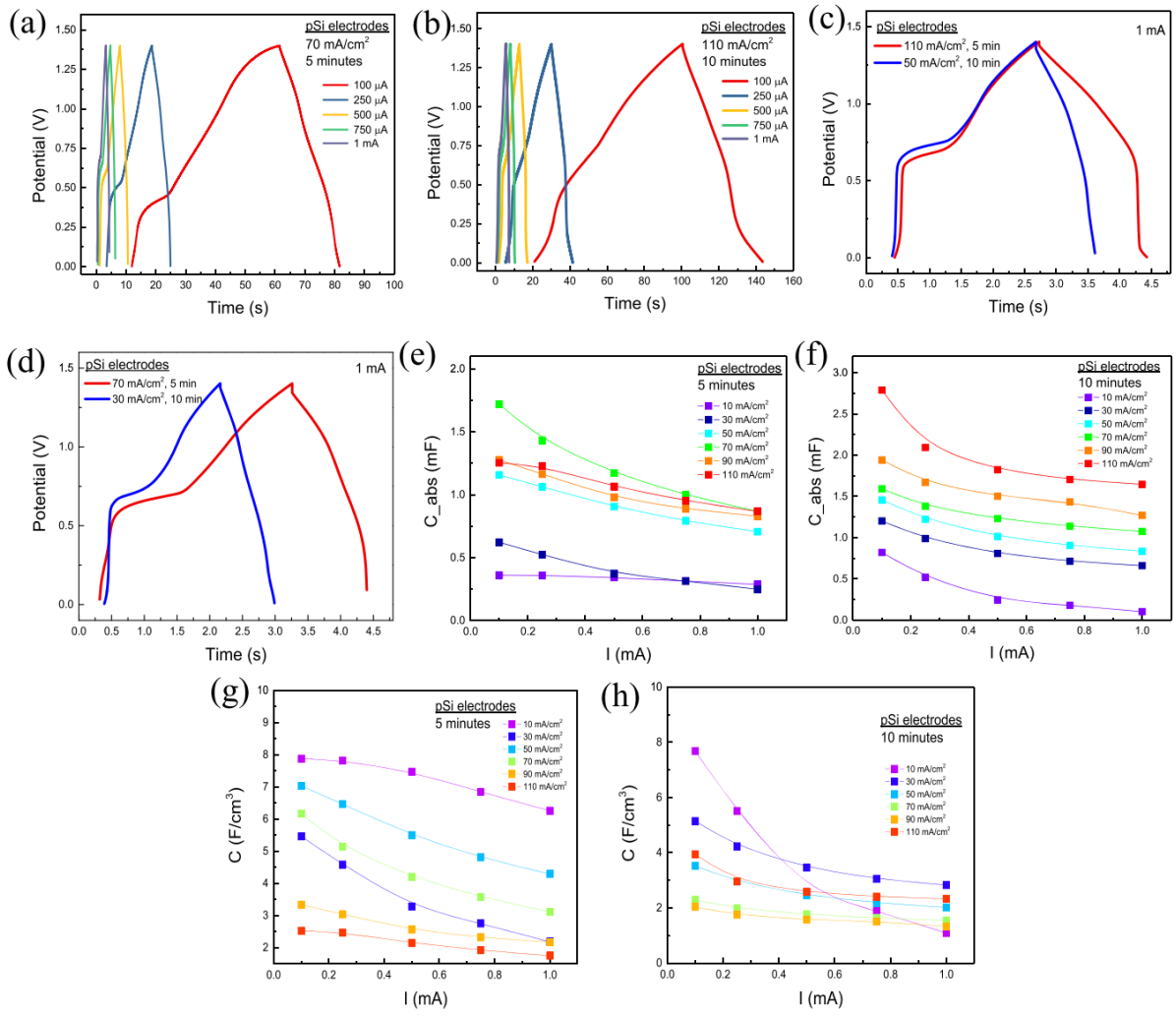

Figure 5. *GDC curves for the symmetric capacitor with electrodes porosified at 110 mA/cm² for 10 min (a) and at 70 mA/cm² for 5 min (b); comparison of the GDC curves for electrodes with the same pore length (c) and same porosity (d); capacitance as a function of current for all 5 min electrodes (e) and for all 10 min electrodes (f); volumetric capacitance symmetric capacitors with electrodes porosified for 5 (g) and 10 min (h)*

Upon initial examination of the charge-discharge curves for each capacitor, it becomes evident, as anticipated, that there is a departure from the triangular-shaped potential characteristic of an ideal capacitor (Figures 5(a,b)). When comparing two electrodes with differing degrees of porosity while maintaining a constant pore length (Figure 5(c)), it is apparent that the electrode subjected to higher current density, and thus greater porosity, exhibits a significantly smaller slope compared to the 10-minute electrode, thereby prolonging the discharging period.

Transitioning to the pair where porosity remains constant but the pore length varies (Figure 5(d)), an initial observation reveals that the electrode with a shorter pore length, 70 mA/cm², takes twice as long to charge compared to the 30 mA/cm² electrode, while displaying the same discharge time.

The calculated capacitances, using the formula from Chapter 3, were initially represented both as absolute values (Figures 5(e) and 5(f)) and as volumetric capacitances (Figures 5(g) and 5(h)) in relation to the applied current. When discussing the capacitance of the device itself, it can be noted that the maximum values are exhibited by the electrodes at 70 mA/cm² for 5 minutes and 100 mA/cm² for 10 minutes.

4.4 **Electrochemical Impedance Spectroscopy Measurements**

Lastly, Electrochemical Impedance Spectroscopy (EIS) measurements were conducted to assess the overall electrical behavior of the supercapacitors. This involved applying a sinusoidal voltage with an amplitude of 10 mV across frequencies ranging from 10 mHz to 1 MHz.

In Figures 7(a) and 7(b) we depict the Nyquist and Bode plots for the two devices previously identified as having the best performances based on absolute capacitance values. Notably, for the 110 mA/cm² electrode, the Nyquist plot displays an increased presence of semicircles, while the Bode plot exhibits smaller peaks. These observations may be attributed to surface nonuniformity and charge transfer processes resulting from the exceptionally large pore length. Although the capacitance appears relatively consistent at lower frequencies, attention is drawn to the significant parallel resistance observed in the 110 mA/cm² electrode.

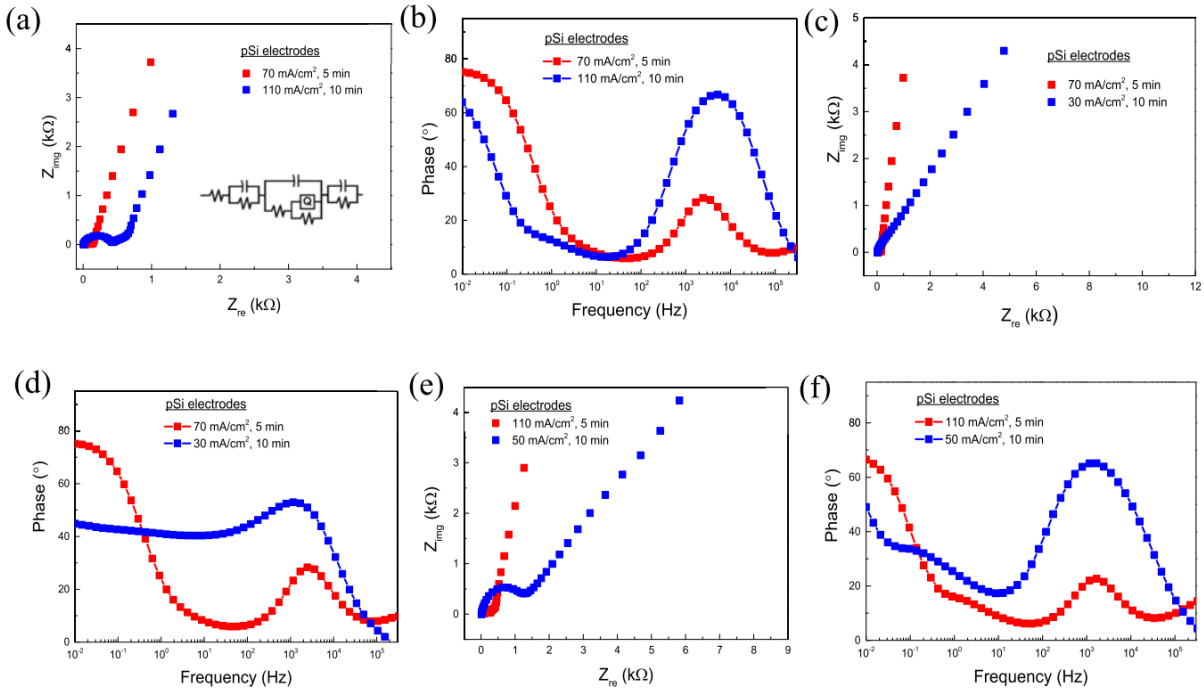

Figure 7. *Comparison of the Nyquist and Bode plots for the electrodes with the best performances (a,b) for the electrodes with the same degree of porosity (c,d) and for the same pore length (e,f)*

Turning our attention to the two electrodes with identical porosity percentages (refer to Figures 7(c) and 7(d)), an initial observation reveals a similar pattern. The electrode subjected to a 10-minute porosification process exhibits an enhanced peak at high frequencies, indicating increased pseudo-capacitance, whereas the one processed for 5 minutes demonstrates superior capacitive behavior at low frequencies. It's evident that longer exposure times result in deeper conductive pathways and a larger surface area, favoring a better

deposition of polymer during the electrodeposition process. While this facilitates an enhanced pseudocapacitive contribution, it also entails a prolonged migration time for charge carriers and a less efficient double layer, as evidenced by the phase at low frequencies [18].

In Figures 7(e) and 7(f), we once again compare two electrodes with the same pore length but different porosity. Notably, the Nyquist plots indicate a similar electrical behavior between the two electrodes, showcasing comparable profiles. However, disparities arise in terms of impedance magnitude and phase, with the electrode featuring higher porosity, namely the 110 mA/cm² electrode, exhibiting a superior phase and higher capacitance value at lower frequencies. These final measurements confirm that electrodes subjected to shorter porosification times offer superior capacitive behavior at low frequencies, with a phase approaching 80° around 10 mHz.

4.5 **Stability Tests on a Porous Silicon Supercapacitor**

Stability tests were conducted on a capacitor assembled using electrodes produced at 50 mA/cm², with a 5-minute exposure time. Impedance data were recorded after 100, 1000, 2000, and 3000 cycles, respectively, as depicted in Figures 8(a) and 8(b). This value was specifically selected as it falls midway between the previously given current density values, providing a general overview of the overall stability.

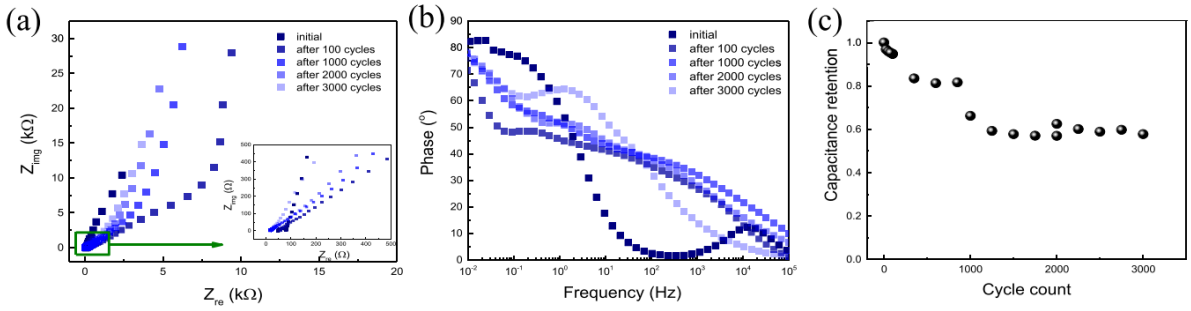

Figure 8. *Nyquist (a) and Bode (b) plots after different periods of charging−discharging cycles; (c) capacity retention.*

In order to measure the charge retention, Figure 8(c) depicts the ratio of areas from the charge-discharge profiles between the initial discharging cycle from 1.5 to 0 V and subsequent equally spaced cycles up to 3000. By the 1000th cycle, the retention has decreased to 80% of its total capacity, indicating the capacitor's continued optimal performance. However, this retention drops to a consistent 60% by the 2000th and 3000th cycles.

Based on the above-mentioned relevant conclusions drawn from this study, the porous Si electrode obtained through anodization at 70 mA/cm^2 was chosen to be subjected to further surface enhancements for an additional improvement of its capacitive performances, which will be presented in the following chapters.

Chapter 4 Bibliography

1. L. Oakes *et al.*, ‘Surface engineered porous silicon for stable, high performance electrochemical supercapacitors’, *Sci Rep*, vol. 3, no. 1, p. 3020, Oct. 2013, doi: 10.1038/srep03020.
2. K. Grigoras, J. Ahopelto, and M. Prunnila, ‘Porous Silicon Supercapacitors’, in *Handbook of Porous Silicon*, Cham: Springer, 2017, pp. 1–11. doi: 10.1007/978-3-319-04508-5_116-2.
3. J.-C. Lin, Y.-C. Liu, S.-H. Lu, H.-N. Yen, and K. Settu, ‘Enhancing the specific capacitance of a porous silicon-based capacitor by embedding graphene combined with three-dimensional electrochemical etching’, *Electrochemistry Communications*, vol. 154, p. 107555, Sep. 2023, doi: 10.1016/j.elecom.2023.107555.
4. ‘Are tomorrow’s micro-supercapacitors hidden in a forest of silicon nanotrees?’, CoLab. Accessed: Dec. 16, 2024. [Online]. Available: https://colab.ws/articles/10.1016%2Fj.jpowsour.2014.05.060
5. Z. Wang *et al.*, ‘Polymers for supercapacitors: Boosting the development of the flexible and wearable energy storage’, *Materials Science and*

Engineering: R: Reports, vol. 139, p. 100520, Jan. 2020, doi: 10.1016/j.mser.2019.100520.

6. N. N. Loganathan, V. Perumal, B. R. Pandian, R. Atchudan, T. N. J. I. Edison, and M. Ovinis, 'Recent studies on polymeric materials for supercapacitor development', *Journal of Energy Storage*, vol. 49, p. 104149, May 2022, doi: 10.1016/j.est.2022.104149.
7. G. Jiang and S. J. Pickering, 'Recycling supercapacitors based on shredding and mild thermal treatment', *Waste Management*, vol. 48, pp. 465–470, Feb. 2016, doi: 10.1016/j.wasman.2015.10.027.
8. N. Xiao *et al.*, 'High-performance supercapacitor electrodes based on graphene achieved by thermal treatment with the aid of nitric acid', *ACS Appl Mater Interfaces*, vol. 5, no. 19, pp. 9656–9662, Oct. 2013, doi: 10.1021/am402686r.
9. P. De *et al.*, 'Role of porosity and diffusion coefficient in porous electrode used in supercapacitors – Correlating theoretical and experimental studies', *Electrochemical Science Advances*, vol. 3, no. 1, p. e2100159, 2023, doi: 10.1002/elsa.202100159.
10. S. Sharma and P. Chand, 'Supercapacitor and electrochemical techniques: A brief review', *Results in Chemistry*, vol. 5, p. 100885, Jan. 2023, doi: 10.1016/j.rechem.2023.100885.
11. H. Wang and L. Pilon, 'Physical interpretation of cyclic voltammetry for measuring electric double layer capacitances', *Electrochimica Acta*, vol. 64, pp. 130–139, Mar. 2012, doi: 10.1016/j.electacta.2011.12.118.
12. X. Lang, A. Hirata, T. Fujita, and M. Chen, 'Nanoporous metal/oxide hybrid electrodes for electrochemical supercapacitors', *Nat Nanotechnol*, vol. 6, no. 4, pp. 232–236, Apr. 2011, doi: 10.1038/nnano.2011.13.
13. N. Singh, S. Tanwar, A. L. Sharma, and B. C. Yadav, 'Advanced cyclic stability and highly efficient different shaped carbonaceous nanostructured electrodes for solid-state energy storage devices',

International Journal of Hydrogen Energy, vol. 47, no. 66, pp. 28254–28271, Aug. 2022, doi: 10.1016/j.ijhydene.2022.06.162.

14. W. Zhao, Z. Zuo, M. Hamza, B. Jia, H. Feng, and B. Mei, 'Physical analysis of self-discharge mechanism for supercapacitor electrode for hybrid electric energy storage system', *Green Energy and Intelligent Transportation*, vol. 2, no. 6, p. 100123, Dec. 2023, doi: 10.1016/j.geits.2023.100123.
15. I. Beyers, A. Bensmann, and R. Hanke-Rauschenbach, 'Ragone plots revisited: A review of methodology and application across energy storage technologies', *Journal of Energy Storage*, vol. 73, p. 109097, Dec. 2023, doi: 10.1016/j.est.2023.109097.
16. Barsoukov, E.; Macdonald, J. R. Impedance Spectroscopy Theory, Experiment, and Applications; John Wiley & Sons, 2005
17. S. Fletcher, V. J. Black, and I. Kirkpatrick, 'A universal equivalent circuit for carbon-based supercapacitors', *J Solid State Electrochem*, vol. 18, no. 5, pp. 1377–1387, May 2014, doi: 10.1007/s10008-013-2328-4.
18. A. R. Bredar, A. L. Chown, A. R. Burton, and B. H. Farnum, 'Electrochemical Impedance Spectroscopy of Metal Oxide Electrodes for Energy Applications', *ACS Applied Energy Materials*, Jan. 2020, doi: 10.1021/acsaem.9b01965.
19. I.-N. Bratosin *et al.*, 'In-Depth Analysis of Porous Si Electrodes for Supercapacitors', *J. Phys. Chem. C*, vol. 125, no. 11, pp. 6043–6054, Mar. 2021, doi: 10.1021/acs.jpcc.0c11035.

Chapter 5

Porous Silicon Modified with Cobalt Hexacyanoferrate Supercapacitor

This chapter focuses on the work accomplished through depositing Cobalt Hexacyanoferrate on the previously described porous Si supercapacitor, with the specific porosity that offered the best capacitive capabilities, namely the one obtained at 70 mA/cm^2 for 5 minutes. It focuses on the process of depositing cobalt hexacyanoferrate nanocubes in addition to the processes previously used to modify porous Silicon electrodes.

5.1 **Fabrication of Porous Silicon Supercapacitors and Deposition of Carbon and Cobalt Hexacyanoferrate**

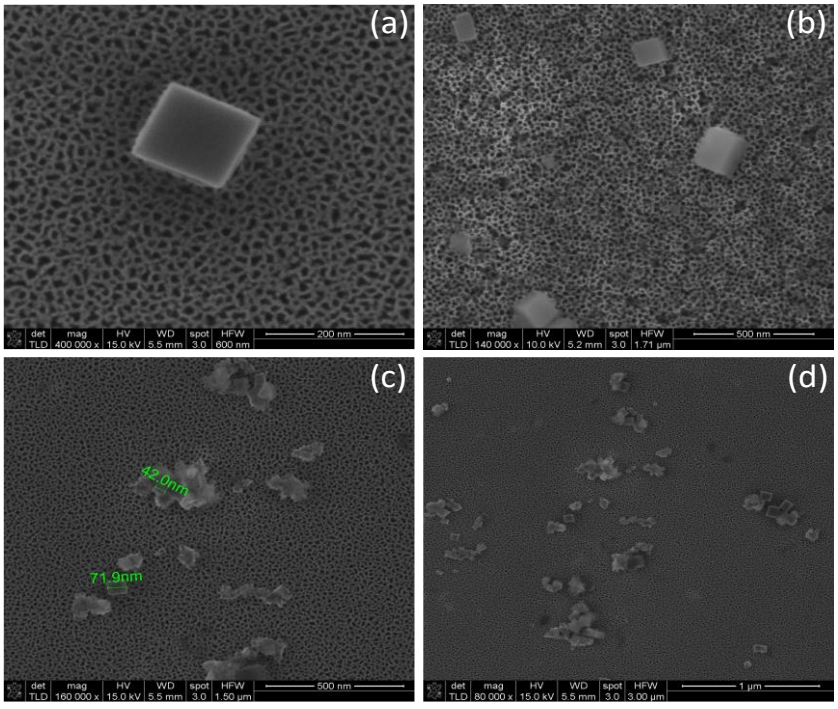

Figure 1. *SEM images of the CoHCF/C/Si electrode at different magnifications*

CoHCF nanocubes were grown on the porous Si's carbonic surface by chronopotentiometry (40 µA, 400 s) which was also carried out in a three-

electrode glass cell with the carbon-hybrid porous silicon as WE, a standard Ag/AgCl electrode and a Pt wire as RE and CE, respectively. The electrolyte bath used for material deposition was a fresh solution containing 5 mM $Co(NO_3)_2 \cdot 6H_2O$, 5 mM $K_3[Fe(CN)_6]$, 10 mM HCl and 1 M K_2SO_4. After electrodeposition, the CoHCF coated p-Si pieces were washed with deionized water, then dried under N_2 [1-3]. The finalized hybrid electrode, denoted as Si+C+CoHCF, had a mass of total active material of about 10 µg.

5.2 **Electrochemical Impedance Spectroscopy Measurements**

Electrochemical impedance spectroscopy (EIS) measurements were conducted over a frequency range of 10 mHz to 100 kHz using a sinusoidal potential signal with an amplitude of 10 mV. These measurements were taken both in the initial state of the device and after subjecting it to 5000 cycles of charge/discharge between 0 – 2.3 V (refer to Figure 2). In the Nyquist plot (Figure 2(a)), the initial

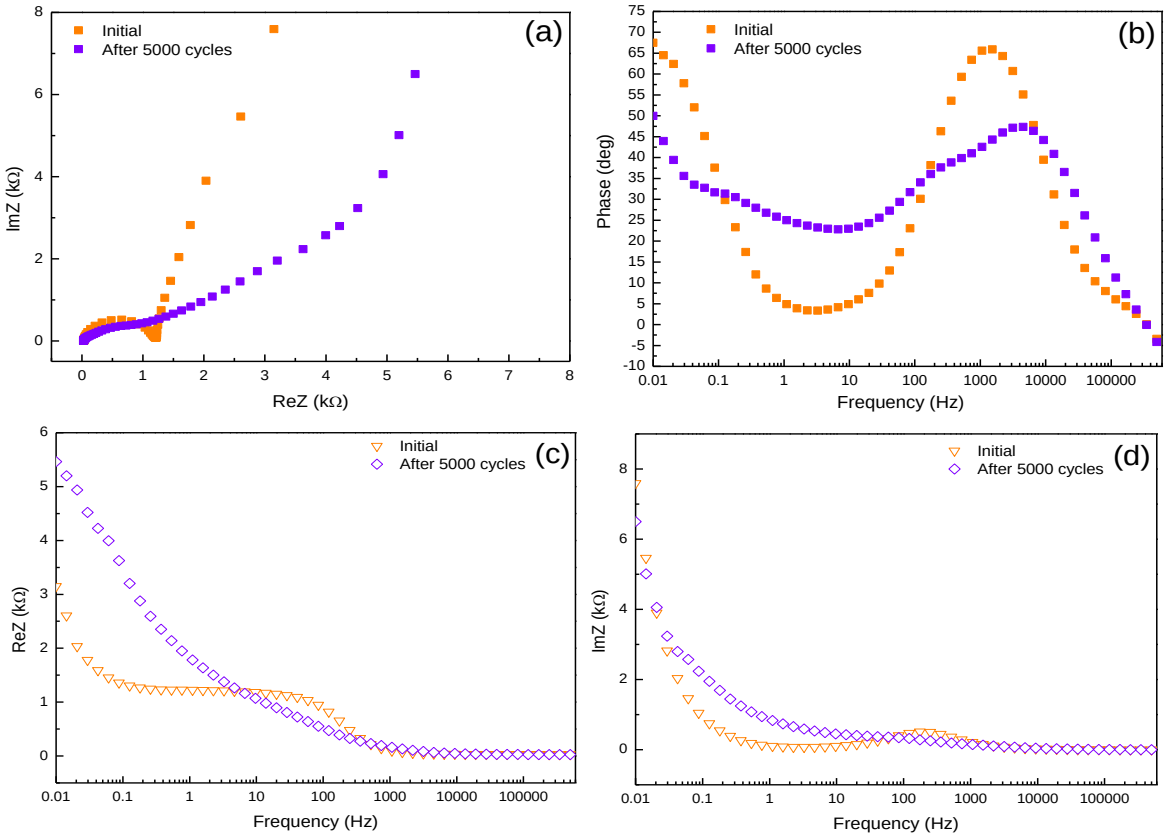

Figure 2. *(a) Nyquist plots before and after C&D; (b) Bode phase angle plots; (c) ReZ(f) and (d) ImZ as function of frequency before and after 5000 cycles for CoHCF/C/Si SSC.*

supercapacitor exhibited a semi-circle in the high-frequency region, indicative of the electrode's capacitance and overall resistance. This was followed by a line nearly parallel to the imaginary axis in the low-frequency region, suggesting the presence of electric double-layer capacitance (EDLC) coupled with charge-transfer phenomena, resembling a Faradaic impedance. This behaviour is attributed to the redox reactions of Fe^{3+}/Fe^{2+} and Co^{3+}/Co^{2+} from the CoHCF material [4,5]. After 5000 cycles, the Nyquist plot displayed a notable increase in the resistance of the device, reflecting significant degradation of the electrode surface. Such modifications, favoured by the redox reactions, are likely responsible for the decline in the capacitive properties.

5.3 **Cyclic Voltammetry Measurements**

The symmetric CoHCF supercapacitor assembly underwent further characterization via cyclic voltammetry, wherein CV scans were conducted across a potential range of 0 to 2.3 V using varying scanning rates, ranging from 5 mV/s to 20 V/s (refer to Figure 3(a)). The resulting CV profiles exhibit a quasi-rectangular shape with discernible changes in slope, indicative of redox reactions occurring at the electrode surface, as anticipated for a pseudocapacitive behaviour [9]. While these redox peaks may not be fully pronounced in all scans, they are notably distinct in the CVs recorded at scanning rates of 2500 and 5000 mV/s, suggesting the presence of Fe^{3+}/Fe^{2+} and Co^{3+}/Co^{2+} redox couples within the CoHCF-based supercapacitor, particularly in the 1.15-1.25 V region. These redox couples are associated with the intercalation/deintercalation of Li^+ ions within the cyano-linked framework of the HCF material (refer to Figure 6(a)).

5.4 **Galvanostatic Charge Discharge Measurements**

Galvanostatic charge-discharge measurements were conducted on the symmetric supercapacitor within the potential range of 0 to 2.3 V, consistent with the

potential window utilized in cyclic voltammetry (CV). Currents ranging from 0.35 mA to 10 mA were applied (refer to Figure 3(b)).

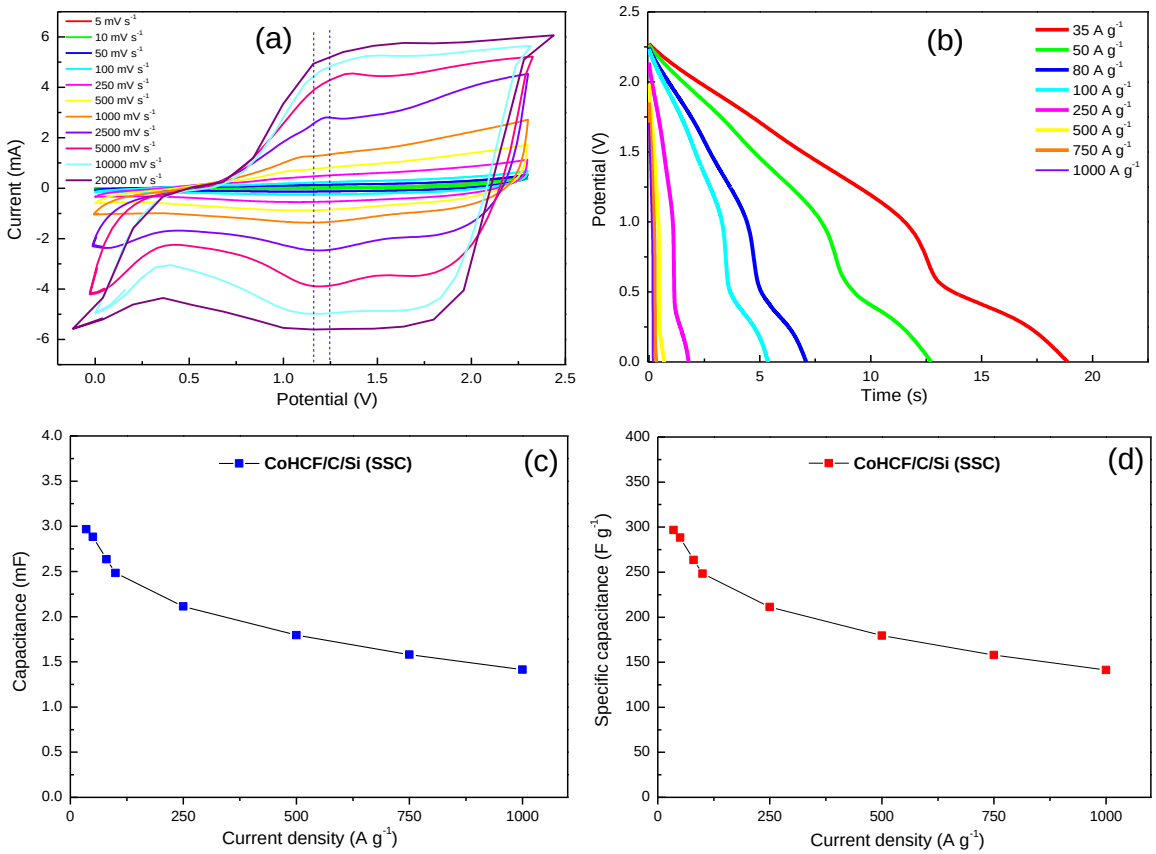

Figure 3. *(a) CV curves at scan rates ranging from 5 mV s^{-1} to 20000 mV s^{-1}; (b) Discharge profiles at different currents for the CoHCF/C/Si supercapacitor; (c) Absolute capacitance and (d) Specific capacitance at various current densities for CoHCF/C/Si supercapacitor.*

The capacitance was computed and represented for each measured current both in absolute terms and relative to the deposited mass (refer to Figures 3(c) and 3(d)). It is evident that the CoHCF/C/Si electrode-based device exhibited a specific capacitance of approximately 300 F/g at a current density of 35 A/g and was capable of achieving a specific capacitance of about 150 F/g, even at a high current density of 1000 A/g.

5.5 **LED Circuit for Testing the Supercapacitor's Performance**

To evaluate the supercapacitor's performance in practical operation, a simple circuit was implemented. Here, the capacitor charges from a 3 V CR2032 battery and subsequently discharges through a variable resistance to illuminate an LED. Therefore, the performance was evaluated based on the duration and brightness of the LED

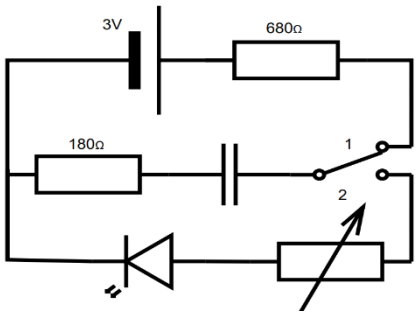

Figure 4. *Circuit schematic for the supercapacitor testing circuit.*

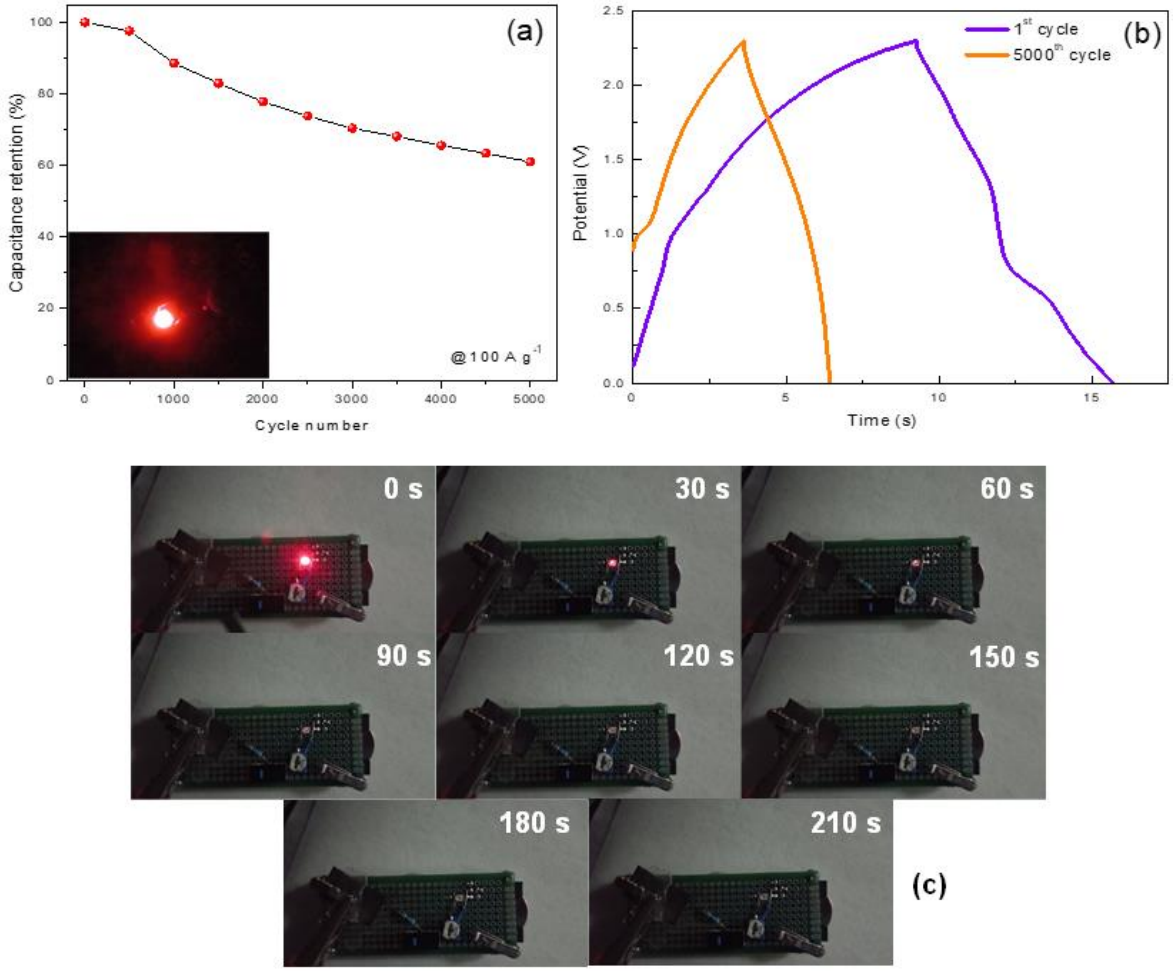

Figure 5. *(a) Capacity retention of the CoHCF/C/Si supercapacitor at 100 A g^{-1} (1 mA) for 5000 cycles (Inset: Picture of an illuminated LED using the CoHCF/C/Si supercapacitor as energy source); (b) GCD profiles before and after 5000 cycles at 1 mA for CoHCF-modified device; (c) Pictures of a powered-up LED at different times during the device's discharge.*

illumination. To switch between charging and discharging modes, a switch with two available positions was utilized. The first position activates the charging

mode, with current flowing through two series resistances: 180 Ω and 680 Ω, respectively. The reason why the 180 Ω resistance was added was as a safety measure to limit the current through the LED if the potentiometer is set in its minimum resistance position, when the supercapacitor is discharged through that LED (Figure 4). The capacitor charges with an initial current of 3.4 mA. The selection of these resistances was made to safeguard both the battery and the LED.

Additionally, Figure 5(b) presents the first and last GCD profiles from the set of 5000 cycles, revealing a noticeable decrease in charging/ discharging times and a distinct change in slope [13]. The initial waveform below 0.5 V is largely absent in the last cycles, indicating that the affected surface of the electrodes primarily contributes to the charge storage mechanism after repeated cycles, reducing the discharge time from approximately 7 s to 3 s at a 1 mA current. Despite the considerable changes observed at the surface level, the device still exhibited excellent specific capacitance with satisfactory cycling stability.

Chapter 5 Bibliography

1. X. Zhu, H. Tao, and M. Li, ‘Co-precipitation synthesis of nickel cobalt hexacyanoferrate for binder-free high-performance supercapacitor electrodes’, *International Journal of Hydrogen Energy*, vol. 45, no. 28, pp. 14452–14460, May 2020, doi: 10.1016/j.ijhydene.2020.02.188.
2. Z. Zhang, J.-G. Wang, and B. Wei, ‘Facile synthesis of Mesoporouscobalt Hexacyanoferrate Nanocubes for High-Performance Supercapacitors’, *Nanomaterials*, vol. 7, no. 8, Art. no. 8, Aug. 2017, doi: 10.3390/nano7080228.
3. F. Zhao *et al.*, ‘Cobalt Hexacyanoferrate Nanoparticles as a High-Rate and Ultra-Stable Supercapacitor Electrode Material’, *ACS Appl. Mater. Interfaces*, vol. 6, no. 14, pp. 11007–11012, Jul. 2014, doi: 10.1021/am503375h.

4. Z. Song *et al.*, ‘Cobalt hexacyanoferrate/MnO2 nanocomposite for asymmetrical supercapacitors with enhanced electrochemical performance and its charge storage mechanism’, *Journal of Power Sources*, vol. 465, p. 228266, Jul. 2020, doi: 10.1016/j.jpowsour.2020.228266.
5. P. Zhu, X. Li, H. Yao, and H. Pang, ‘Hollow cobalt-iron prussian blue analogue nanocubes for high-performance supercapacitors’, *Journal of Energy Storage*, vol. 31, p. 101544, Oct. 2020, doi: 10.1016/j.est.2020.101544.
6. Z. Song *et al.*, ‘Charge storage mechanism of copper hexacyanoferrate nanocubes for supercapacitors’, *Chinese Chemical Letters*, vol. 31, no. 5, pp. 1213–1216, May 2020, doi: 10.1016/j.cclet.2019.07.022.
7. I.-N. Bratosin *et al.*, ‘Graphitized porous silicon decorated with cobalt hexacyanoferrate nanocubes as hybrid electrode for high-performance supercapacitors’, *Electrochimica Acta*, vol. 424, p. 140632, Aug. 2022, doi: 10.1016/j.electacta.2022.140632.
8. U. Shuaib, T. Hussain, R. Ahmad, F. E. Mubarik, S. Ahmad, and I. Shakir, ‘Chemically synthesized cobalt oxide incorporated copper hexacyanoferrate (Co3O4–CuHCF) composite as an efficient supercapacitor electrode material’, *J Appl Electrochem*, vol. 54, no. 2, pp. 245–256, Feb. 2024, doi: 10.1007/s10800-023-01957-1.
9. D. Gromadskyi, V. Chervoniuk, and S. Kirillov, ‘Cyclic voltammetric study of tin hexacyanoferrate for aqueous battery applications’, *Journal of Electrochemical Science and Engineering*, vol. 6, no. 3, Art. no. 3, Sep. 2016, doi: 10.5599/jese.289.
10. B. M. Pires *et al.*, ‘Characterization of porous cobalt hexacyanoferrate and activated carbon electrodes under dynamic polarization conditions in a sodium-ion pseudocapacitor’, *Journal of Energy Chemistry*, vol. 54, pp. 53–62, Mar. 2021, doi: 10.1016/j.jechem.2020.05.045.

11. J. Chen, K. Huang, and S. Liu, ‘Insoluble metal hexacyanoferrates as supercapacitor electrodes’, *Electrochemistry Communications*, vol. 10, no. 12, pp. 1851–1855, Dec. 2008, doi: 10.1016/j.elecom.2008.07.046.
12. R. S. Babu, A. L. F. de Barros, M. de Almeida Maier, D. da Motta Sampaio, J. Balamurugan, and J. H. Lee, ‘Novel polyaniline/manganese hexacyanoferrate nanoparticles on carbon fiber as binder-free electrode for flexible supercapacitors’, *Composites Part B: Engineering*, vol. 143, pp. 141–147, Jun. 2018, doi: 10.1016/j.compositesb.2018.02.007.
13. C. D. Wessells, R. A. Huggins, and Y. Cui, ‘Copper hexacyanoferrate battery electrodes with long cycle life and high power’, *Nat Commun*, vol. 2, no. 1, p. 550, Nov. 2011, doi: 10.1038/ncomms1563.

Chapter 6

TiN Supercapacitor: Sometimes Research is not Intentional, it's Serendipitous

6.1 The Conceptualization Process of the Presented Supercapacitor Surface

This chapter deals with porous Si modified with a layer of carbon composite underneath going through an additional modification process in order to deposit an extra, continuous layer on top of it as a multi-layer system (Schematic 1), which is meant to present a better stability due to this fail-safe mechanism implemented.

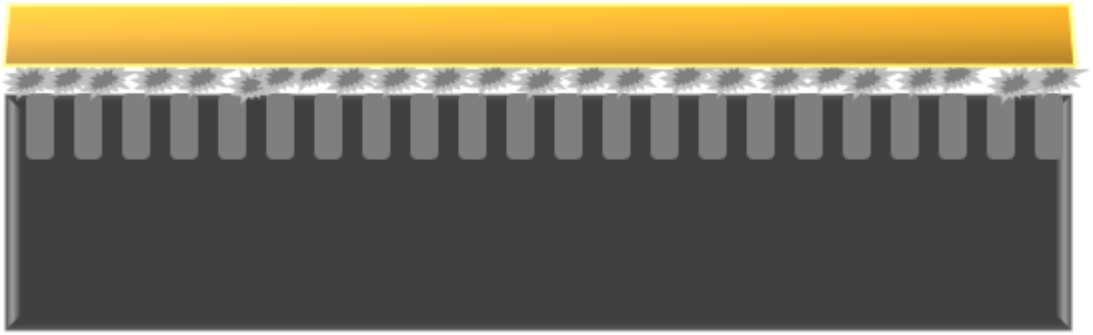

***Schematic 1**. A visual representation of the resulting supercapacitor structure: dark grey – Doped Silicon layer, light grey – pores etched in the Silicon surface, formation on top of the Silicon layer – deposited polymer which was turned into carbon composites through thermal treatment, golden layer – TiN layer deposited on top*

The resulting supercapacitor has been subjected to tens of thousands of charge-discharge cycles in order to verify that the implemented fail-safe system works and the stability is improved. EIS, as well as CV have been used in addition of GCD in order to explain the physical phenomena behind the evolution of the supercapacitor's performance throughout this intense process of cycling.

6.2 **TiN Supercapacitor Fabrication Process**

TiN films were deposited directly onto the graphitized p-Si pieces as substrates by RF magnetron sputtering (MS) with the PlasmaLab System 400 from Oxford Instruments, Abingdon, UK. The TiN layer deposition was carried out reactively, from a 154 mm-diameter Ti target (Testbourne Ltd., Basingstoke, UK), by introducing both Ar (99.999% purity) and N_2 (99.9999% purity) as nitrogen precursor in the reaction chamber and igniting a RF (13.56 MHz) plasma. A base pressure of 10^{-7} Torr is reached prior to the deposition, after which Ar and N_2 are introduced into the chamber and the plasma is ignited at 30 mTorr. After ignition, the pressure is lowered to the desired value. The nitrogen percentage in the gas mixture was ~9%, while the pressure and RF power were kept constant during the deposition at ~2 mTorr and 350 W, respectively. TiN depositions were carried out at a substrate temperature of 50 °C. The swipe number during the deposition was varied to achieve different thickness values for the TiN layer, as follows: 450, 830, 1300 and 1650 swipes to obtain 50, 100, 150

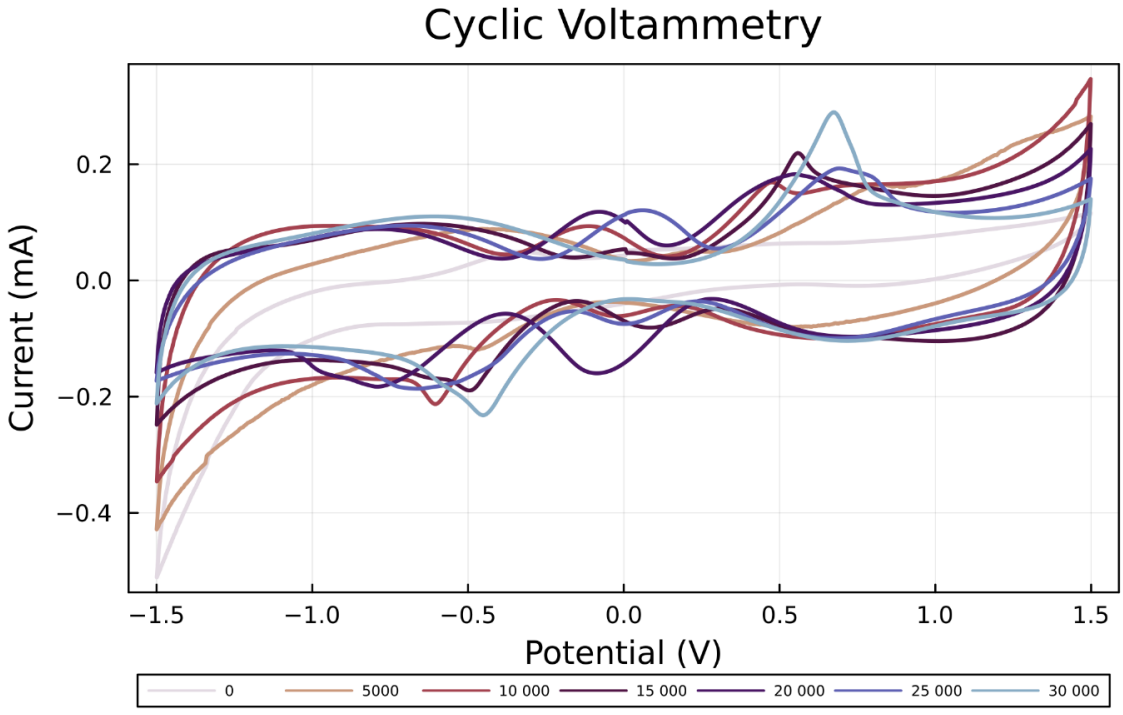

Figure 2. *Cyclic Voltammograms performed every 5 000 cycles at 50 mV/s scan rate*

and 200 nm, respectively. Thus, the discussed electrodes are denoted as Ti 50, Ti 100, Ti 150 and Ti 200, after the intended thickness of TiN films.

6.3 **Developing a Quantitative Relation Between Cyclic Voltammetry and Electrochemical Impedance Spectroscopy**

Cyclic voltammetry measurements were performed between -1.5 V and 1.5 V at different scan rates, 50, 100, 250, 500, 1000 mV/s. Due to the possibility of coupling it with EIS measurements, the CV measurements made at 50 mV/s are presented in Figure 2.

Cyclic voltammetry (Figure 2) at 50 mV/s presents a few areas of interest, mainly around 0 V, +/- 1.5 V and +/- 0.5 V. In the initial voltammogram, only the -1.5 V portion is visible, which points to some chemical compound formed at the surface during the fabrication, when the surface is being reduced in a redox reaction, and the significantly higher current value compared to the average current indicates that some form of corrosion is taking place [8]. Considering that the electrodes are made of porous Si + a layer of carbon, which are covered by a layer of TiN, these results indicate that the phosphoric acid might be attacking the TiN layer [9].

After 30 000 C/D cycles, SEM measurements were performed on one of the two electrodes used (Figure 3). What has been predicted by CV was revealed to be the case in Figure 3(a), where it can be clearly seen that the top layer of TiN has been “broken” into a scale-like formation. Figures 3 (c) and (d) show a magnified look of the supercapacitor’s surface, where patches of dried-up electrolyte, as well as the porous Si area underneath are visible.

Figures 4(a) and 4(b) display the current values at +/-1.5 V in more details. It can be observed that in both cases, as the number of cycles increases, the amount of charges originating from over oxidation/reduction decreases. This

observation can be explained as most of the corrosion of the TiN layer happened in the first 10 000 cycles.

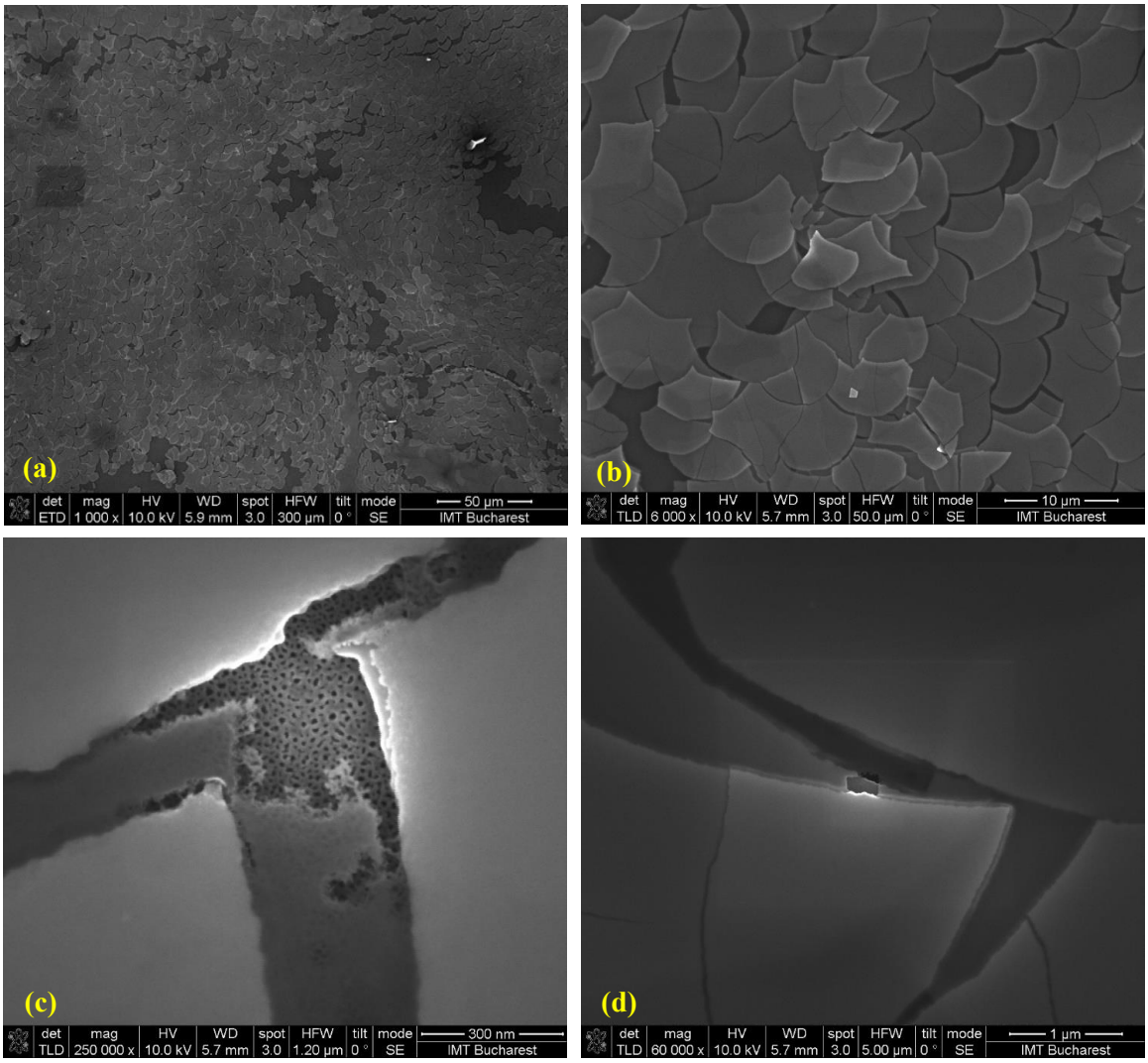

Figure 3. *(a) SEM top view of the TiN layer after cycling; (b) Closer look at the TiN layer; (c) Top view of the porous Si layer underneath the TiN layer; (d) A view of the electrolyte trapped between scales of TiN.*

Figures 4(c) and 4(d) present the computed maximum and minimum current values around the area of interest for both CV and EIS, which is a redox reaction present around 0 V in the CV curves. Because EIS uses a sinusoidal signal with an amplitude of 10 mV and the lowest frequency of the applied signal is around 10 mHz, in the EIS analysis for this region, there is also a pseudo-capacitive potential-dependent component.

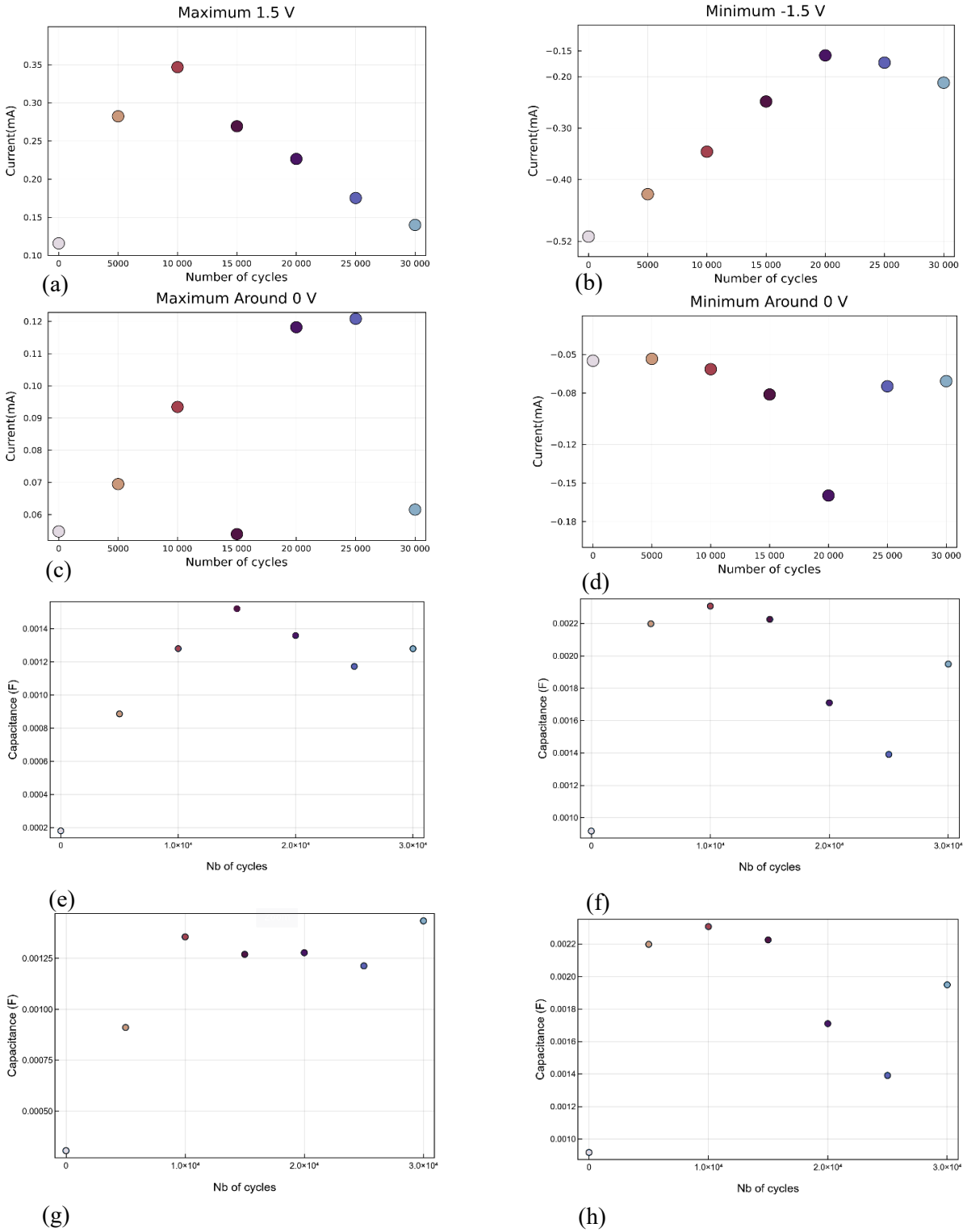

Figure 4. *(a) Local maximum value for each cycles recording vs number of cycles at 1.5 V; (b) local minimum at -1.5 V; (c) local maximum around 0 V; (d) local minimum around 0 V; (e) Capacitance value calculated in the first quadrant; (f) second quadrant; (g) third quadrant and (h) fourth quadrant*

Figure 5 shows the Nyquist graphs at each batch of cycles. Together with Figure 6, which illustrates data pertaining to Bode graphs, it tells a story of what happened to the two electrodes, which will be unfolded by linking together the CV analysis with the EIS analysis.

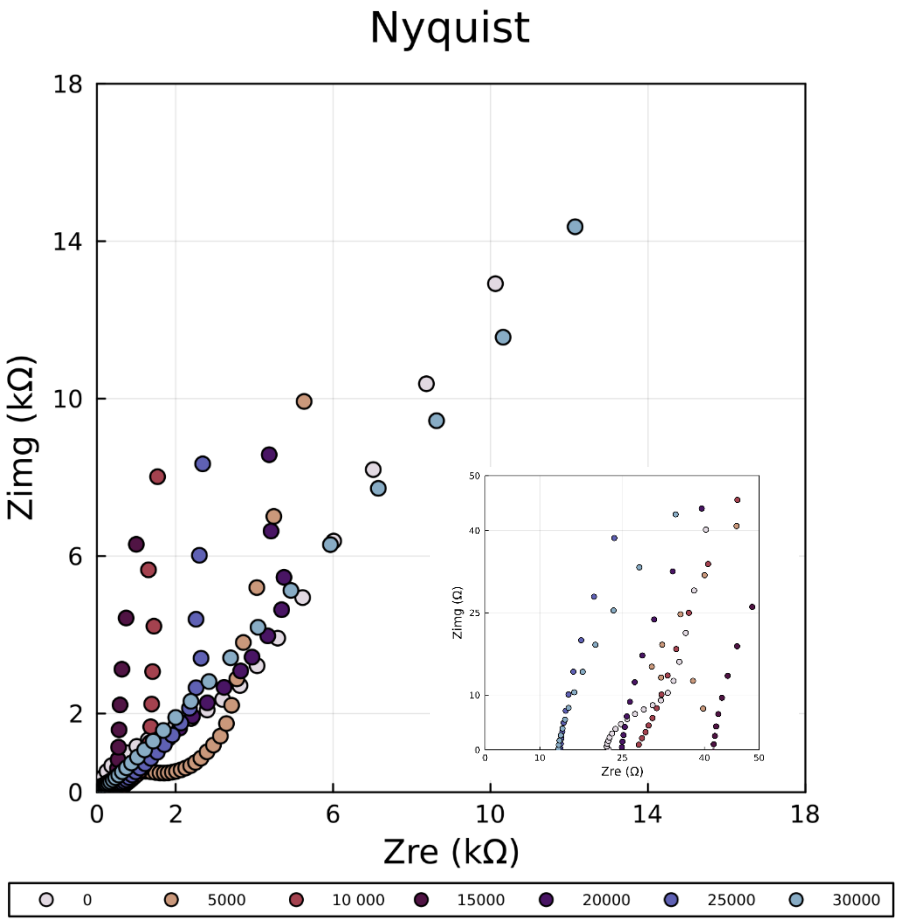

Figure 5. *Nyquist for each cycle iteration, with a zoom in (to the right)*

Moving further, for the sake of simplicity any frequency below 10 Hz will be called as being in the low frequencies region (LF) and any frequency above 10 Hz will be called as being in the high frequencies region (HF).

Because TiN completely covers the porous and the carbon layers, it is safe to assume that initially most of the charge storage contribution comes from the TiN layer, specifically the ECDL capacitance at the surface. After 5000 cycles,

Figure 6(a) shows a slight increase in the phase difference at LF. Since for each iteration two peaks can be differentiated, indicative of parallel RC circuits, the behaviour can be modelled as being a circuit with a series resistance and two parallel RC circuits in series, one corresponding to the LF behaviour and the other to the HF behaviour.

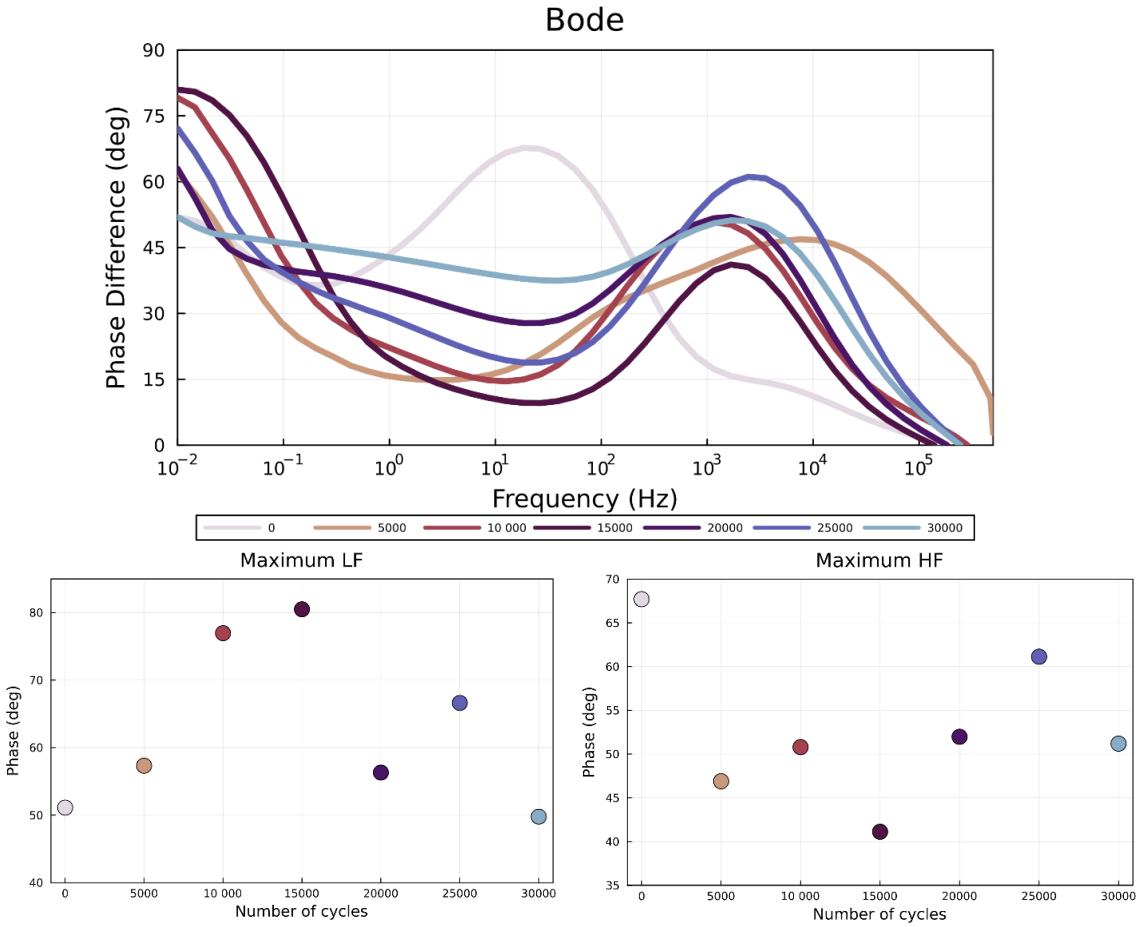

Figure 6. *(a) Bode for each cycle iteration; (b) Local maxima taken for each iteration above 10 Hz; (c) Local maxima taken for each iteration below 10 Hz.*

Therefore, the phase difference can be treated separately in each region as the tangent between the two impedances:

$$\tan(\theta) = \frac{Xc}{R},$$

where Xc is the capacitive reactance and R the resistance.

Thus, a change in the phase difference between the input potential and the output current can be caused by a change in either resistance or capacitance or both. Figures 6(b) and 6(c) present the evolution of the phase differences in more details in each respective region.

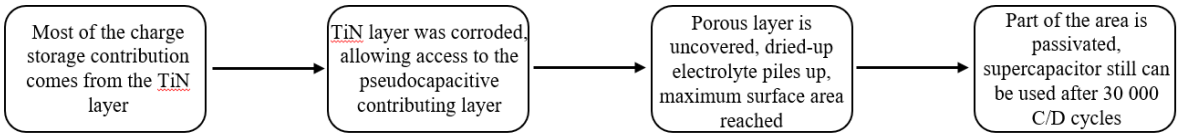

Schematic 2. *A diagram showcasing the supercapacitor's evolution throughout the charging-discharging cycling process*

CV together with EIS have shown that throughout the C/D cycling the supercapacitor has been subjected to, it has gone from a TiN capacitor, to a TiN modified surface + pseudocapacitive layer + porous Si to a TiN modified surface + dried electrolyte dielectric + passivated layer + porous Si. These modifications to the surface caused by the electrolyte can be coupled with the potential application. The C/D cycles and the mechanical stress can explain how the capacitance of the device ends up increasing in value, after passing through a maximum value where the optimal exposure to the surface and redox active layer was achieved (Schematic 2).

6.4 **Galvanostatic Charge Discharge Measurements of TiN Supercapacitors**

The last measurement to be discussed is the one most indicative of the supercapacitor's performance, namely GCD. The device was subjected to 30 000 charge-discharge cycles between 0 and 2 V at a 0.5 mA current. While CV measurements indicate that the operation of the structure is preferable to occur under 1.5 V, the device was pushed forward in order to test the TiN layer and to investigate what would happen to it under extreme conditions. Figures 7(a) and 7(b) show a charging, respectively a discharging curve each 5000 cycles.

What was concluded by the previous measurements is confirmed by the discharging time in Figure 7(b). The initial state offers the lowest discharging time, with the supercapacitor showing a steady increase in performance up to 15 000 cycles, after which a steady decline is observed up to 30 000 cycles.

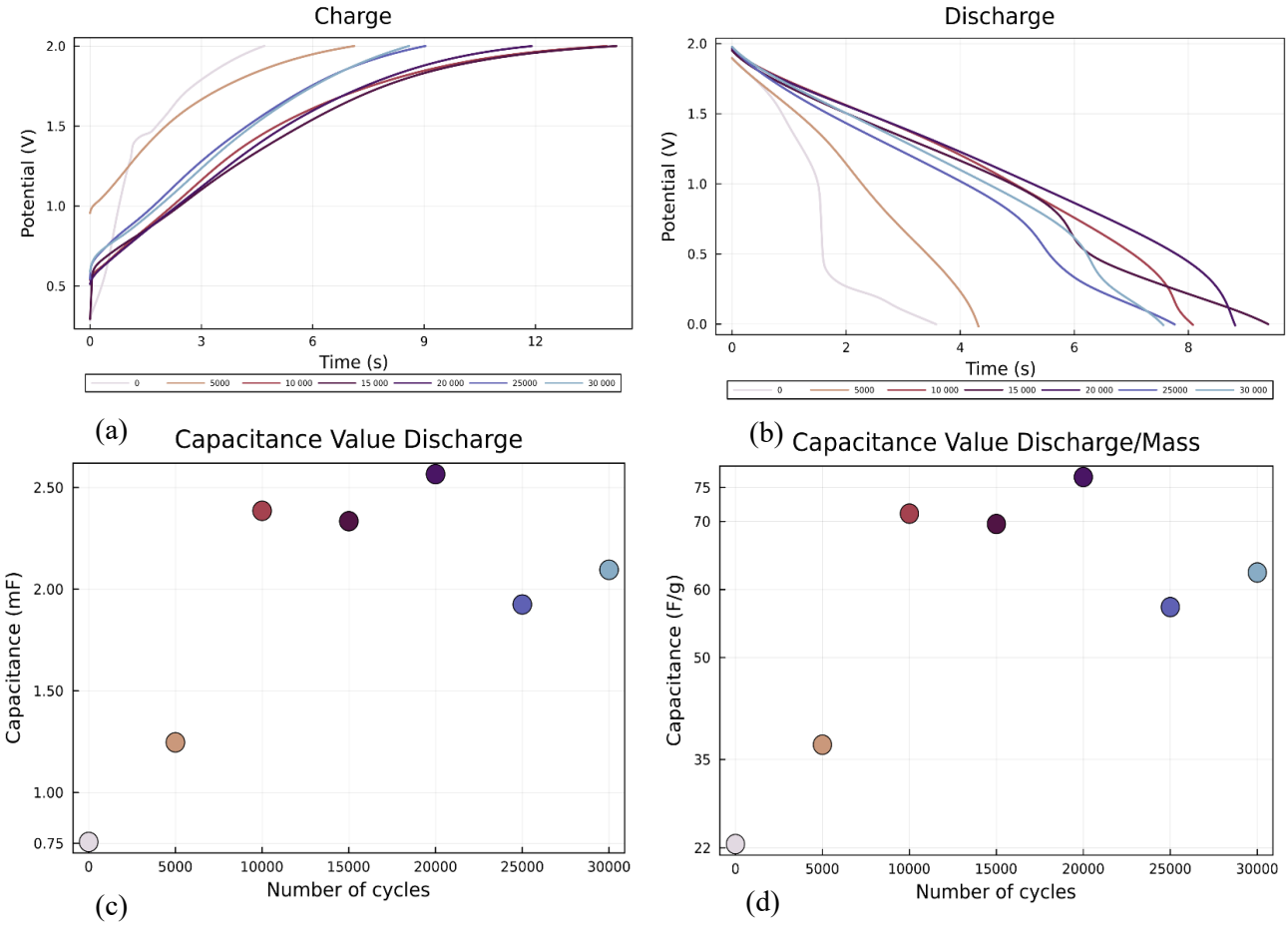

Figure 7. *(a) Charging curves for each cycle iteration @ 0.5 mA; (b) Discharging curves for each cycle iteration at 0.5 mA; (c) Capacitance calculated from discharge curves in absolute values; (d) Same capacitance in F/g.*

The absolute capacitance was calculated and plotted in Figure 7 (c). The mass capacitance was calculated by using the TiN's layer measured density, 4.47 g cm^{-3}, its surface area, 0.5 cm^2, and length, 150 nm, and it was determined to be 33.525 µg (Figure 7(d)).

Chapter 6 Bibliography

1. Y. Zhao and X. Zhang, 'In situ activation graphitization to fabricate hierarchical porous graphitic carbon for supercapacitor', *Sci Rep*, vol. 11, no. 1, p. 6825, Mar. 2021, doi: 10.1038/s41598-021-85661-0.
2. S. Tang *et al.*, 'Preparation of Titanium nitride nanomaterials for electrode and application in energy storage', *Results in Physics*, vol. 7, pp. 1198–1201, Jan. 2017, doi: 10.1016/j.rinp.2017.03.006.
3. N. Parveen, M. O. Ansari, S. A. Ansari, and P. Kumar, 'Nanostructured Titanium Nitride and Its Composites as High-Performance Supercapacitor Electrode Material', *Nanomaterials (Basel)*, vol. 13, no. 1, p. 105, Dec. 2022, doi: 10.3390/nano13010105.
4. J. Arpa, K. Rechendorff, P. S. Wismayer, and B. Mallia, 'Ultra-porous titanium nitride as a dual-action supercapacitor for implantable neural interfacing electrodes', *Materials Chemistry and Physics*, vol. 289, p. 126435, Sep. 2022, doi: 10.1016/j.matchemphys.2022.126435.
5. N. Sun *et al.*, 'Tailoring Surface Chemistry and Morphology of Titanium Nitride Electrode for On-Chip Supercapacitors', *ACS Sustainable Chem. Eng.*, vol. 8, no. 21, pp. 7869–7878, Jun. 2020, doi: 10.1021/acssuschemeng.0c00977.
6. J. Bezanson, A. Edelman, S. Karpinski, and V. B. Shah, "Julia: A Fresh Approach to Numerical Computing," SIAM Review, vol. 59, no. 1, pp. 65–98, Jan. 2017, doi: 10.1137/141000671
7. T. Breloff, "Plots.jl." Zenodo, Aug. 30, 2023. doi: 10.5281/zenodo.8300728
8. Y. Xie, Y. Wang, and H. Du, 'Electrochemical capacitance performance of titanium nitride nanoarray', *Materials Science and Engineering: B*, vol. 178, no. 20, pp. 1443–1451, Dec. 2013, doi: 10.1016/j.mseb.2013.09.005.
9. B. M. Gray, A. L. Hector, M. Jura, J. R. Owen, and J. Whittam, 'Effect of oxidative surface treatments on charge storage at titanium nitride surfaces

for supercapacitor applications', *J. Mater. Chem. A*, vol. 5, no. 9, pp. 4550–4559, Feb. 2017, doi: 10.1039/C6TA08308K.

10. T. Zheng *et al.*, 'Sputtered titanium nitride films on titanium foam substrates as electrodes for high-power electrochemical capacitors', *ChemElectroChem*, vol. 5, no. 16, Art. no. 16, Aug. 2018.
11. D. Yang, C. Liu, X. Liu, M. Qi, and G. Lin, 'EIS diagnosis on the corrosion behavior of TiN coated NiTi surgical alloy', *Current Applied Physics*, vol. 5, no. 5, pp. 417–421, Jul. 2005, doi: 10.1016/j.cap.2004.11.002.
12. J. R. Abbott, A. Joshi-Imre, and S. F. Cogan, 'In Vitro Electrochemical Properties of Titanium Nitride Neural Stimulating and Recording Electrodes as a Function of Film Thickness and Voltage Biasing', *Annu Int Conf IEEE Eng Med Biol Soc*, vol. 2021, pp. 6647–6650, Nov. 2021, doi: 10.1109/EMBC46164.2021.9630715.

Chapter 7

Circuit Modelling for Porous Silicon Supercapacitors

In the following pages I will present the formalism I have developed so far towards achieving a plausible and correct circuit model for supercapacitors. This work was done in the Julia programming language [1] using the following packages: Plots.jl [2], DataInterpolations [3], Optimization.jl [4], DataFrames.jl [5], CSV.jl [6], PrettyTables.jl [7], GR.jl [8].

7.1 **Software used for data plotting**

Before moving on to modelling, data must be turned into graphs. In developing the algorithm for circuit modelling, and for supercapacitor analysis in general, a significant number of data files piled up, prompting a different approach to plotting all the graphs needed for this modelling. Before I started the modelling, I wrote a few programs in the programming language Julia which will do the graphics automatically once the respective data file is selected. The graphs in question can be found at https://github.com/Ir1n-a.

7.2 **Measurements for data modelling**

While ultimately the algorithm's job is to model the behaviour of a supercapacitor into an equivalent circuit, starting directly with supercapacitor data in programming in the said model would make the task more daunting than it already is or should be. In order to validate an algorithm's prediction, I should already know what the result should be, otherwise I'm pretty much working in the dark. So, because of this I first performed EIS measurements on classical RC circuits that I have soldered myself with components whose values are already known, literally listed on the package. I've assembled multiple types of RC

circuits while also trying to follow the form of what a specific supercapacitor EIS graph looks like.

Figure 1 shows how the Nyquist graph of a porous Silicon supercapacitor looks like. Three different regions stand out: region one, for which *Zre* ϵ (0,2000) Ω, region two, with *Zre* ϵ [2000,6000) Ω, and region three *Zre* ≥ 6000 Ω. Region one is similar to a Nyquist graph of a parallel RC circuit (Figures 2 (a,c)), and regions two and three are similar to a parallel RC circuit in series with a RC ladder circuit (Figures 2 (b,d)), so combining the two circuits in series should give a Nyquist graph similar to that of a capacitor, which it does.

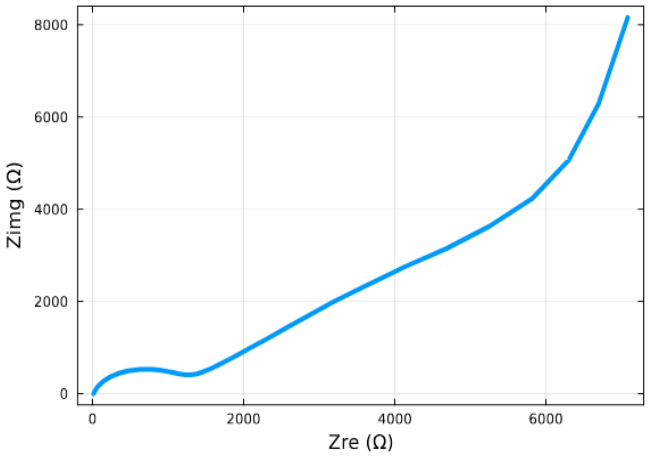

Figure 1. *Nyquist characteristic of a porous Silicon supercapacitor*

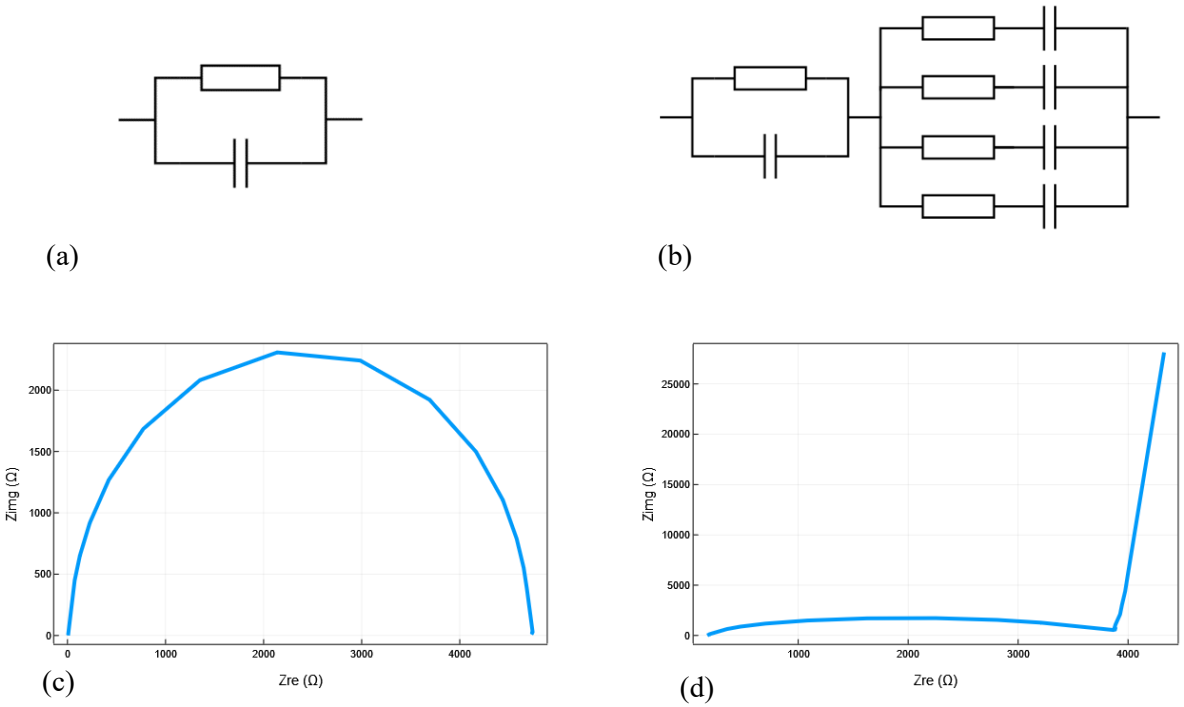

Figure 2. *Schematics of (a) a parallel RC circuit, and (b) a parallel RC circuit connected in series with an RC ladder circuit. (c,d)Nyquist graphs for measured circuits of types (a,b), respectively.*

In order to model region one, the model discovery program needs to be able to recognize that this particular shape corresponds to a parallel RC circuit, to determine the parameters from the graph, to introduce constraints for the possible parameters and to have a fitting stage where the theoretical model obtained is plotted against and compared to the experimental data. Therefore, I have decided to solder and measure a circuit made out of four parallel RC circuits in series. The reason why I chose four instead of one or two was to make it harder for the program to discover and calculate all of them, for there is a possibility for supercapacitor Nyquist graphs to contain more than one single RC circuit in region one.

Figure 3 (a) shows the soldered device and Figure 3 (b) shows the resulting Nyquist graph from EIS measurements performed on the presented circuit. For clarity, the circuit's schematic, Figure 3 (c), was also included. The circuit test was measured, next a theoretical model and a parameter determination algorithm was needed to check if the final program could possibly guess the schematic, as well as the values for each electronic component present in the circuit.

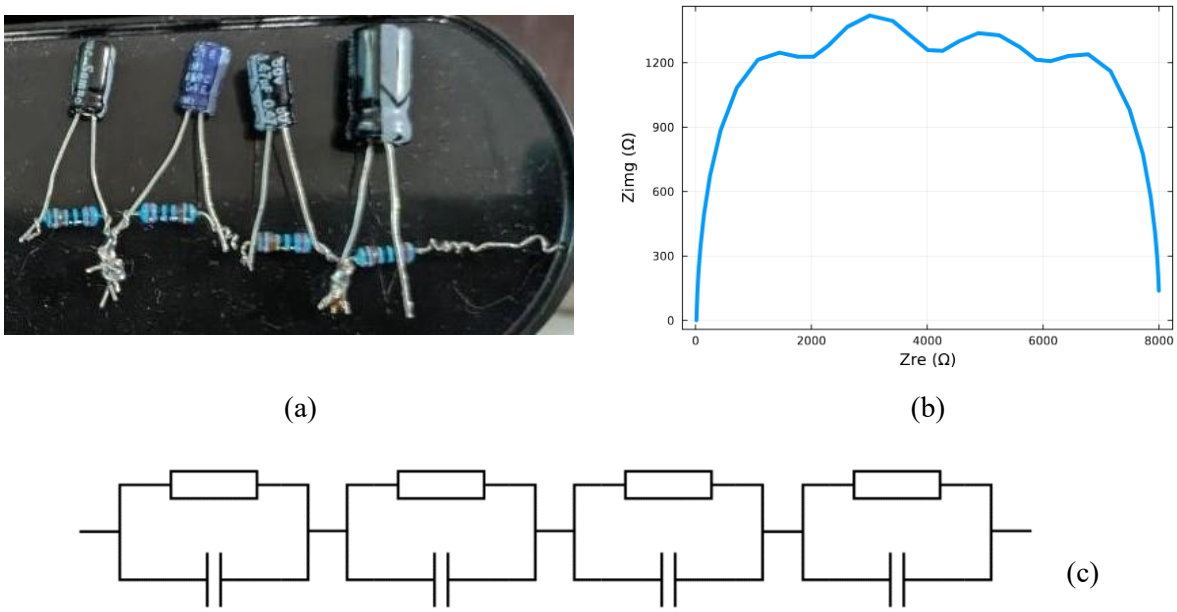

Figure 3. *(a) Physical circuit. (b) Nyquist graph of the circuit. (c) Circuit's schematic.*

7.3 **Theoretical model used**

The measuring apparatus determines the total impedance $Z = Zre + jZimg$ from $\frac{V(t)}{I(t)}$, which is a complex number, and the Nyquist graph plots its imaginary part on y and its real part on x. The circuit in question consists of 4 parallel RCs in series, so, naturally, the real and imaginary part should be determined for one parallel RC circuit first. For this RC circuit, the impedances for the resistance R and capacitance C are, respectively

$$Z_R = R \quad \text{and} \quad Z_C = \frac{1}{j\omega C},$$

with ω-angular frequency, so that for the parallel circuit,

$$\frac{1}{Z} = \frac{1}{Z_R} + \frac{1}{Z_C} = \frac{1}{R} + j\omega C = \frac{1 + j\omega RC}{R}$$

or

$$Z = \frac{R}{1 + j\omega RC} = \frac{R - j\omega R^2 C}{1 + \omega^2 R^2 C^2}.$$

This is the total impedance for one RC circuit, and when adding three more of them, since they are in series, the total impedances will just have to be added. We have for the nth element

$$Z_n = \frac{R_n - j\omega {R_n}^2 C_n}{1 + \omega^2 {R_n}^2 {C_n}^2}, \quad Zre_n = \frac{R_n}{1 + \omega^2 {R_n}^2 {C_n}^2}, \quad Zimg_n = \frac{-\omega {R_n}^2 C_n}{1 + \omega^2 {R_n}^2 {C_n}^2}$$

and thus for the circuit

$$Z_i = \sum_{i=1}^{4} \frac{R_i - j\omega {R_i}^2 C_i}{1 + \omega^2 {R_i}^2 {C_i}^2}, \quad Zre_i = \sum_{i=1}^{4} \frac{R_i}{1 + \omega^2 {R_i}^2 {C_i}^2}, \quad Zimg_i = \sum_{i=1}^{4} \frac{-\omega {R_i}^2 C_i}{1 + \omega^2 {R_i}^2 {C_i}^2}$$

A function made out of the formula for the total imaginary part plotted against the formula for the total real part should fit the experimental data, that is if the parameter determination and optimization algorithms are accurate enough to hit

their target values, which moves the algorithm to the parameter determination section.

7.4 **Parameter determination algorithm**

In order to make sure the optimization step converges to the parameter values it should discover, an accurate parameter determination is paramount. So how exactly will this be achieved?

In the Nyquist plot (Figure 4), there are a few notable points that could be used for parameter determination, such as at the maximum value for *Zimg*, where the relation $\omega RC = 1$ must be fulfilled, as well as at the lowest value for *Zre*, $Zre_{min} = Rs$ (series resistance), and for the maximum value for $Zre_{max} = Rp$. Looking at these relations, a picture starts to form on what the algorithm must do to determine the circuit's parameters.

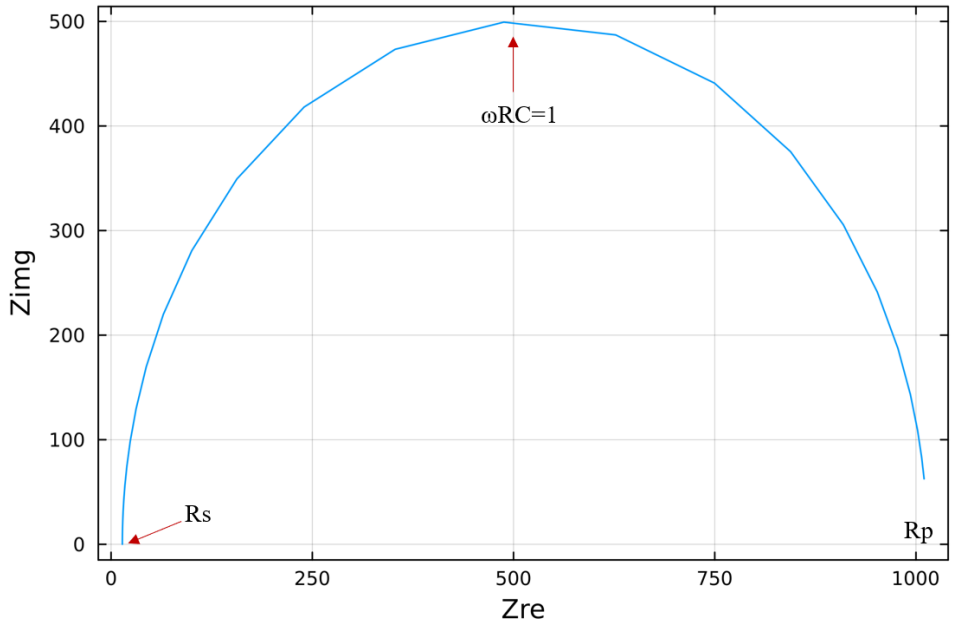

Figure 4. *Plot of theoretical formulas for Zre and Zimg and marks for points of interest.*

To compare the results, I plotted the experimental data, the theoretical model using the values determined by the parameter determination section and the theoretical model using the values determined by the optimization algorithm

(Figure 5). Optimization.jl is a Julia package providing a unified interface for defining and solving mathematical optimization problems, such that one can use several optimization algorithms with the same syntax. In order to fit the data, an objective function was defined describing how far the experimental values are from the theoretical predictions. Thus, the mathematical optimization problem consists of finding the parameters that minimize the value of this function. To achieve this, I used the LBFGS [9] algorithm in Optimization.jl with the starting point given by the parameter determination algorithm.

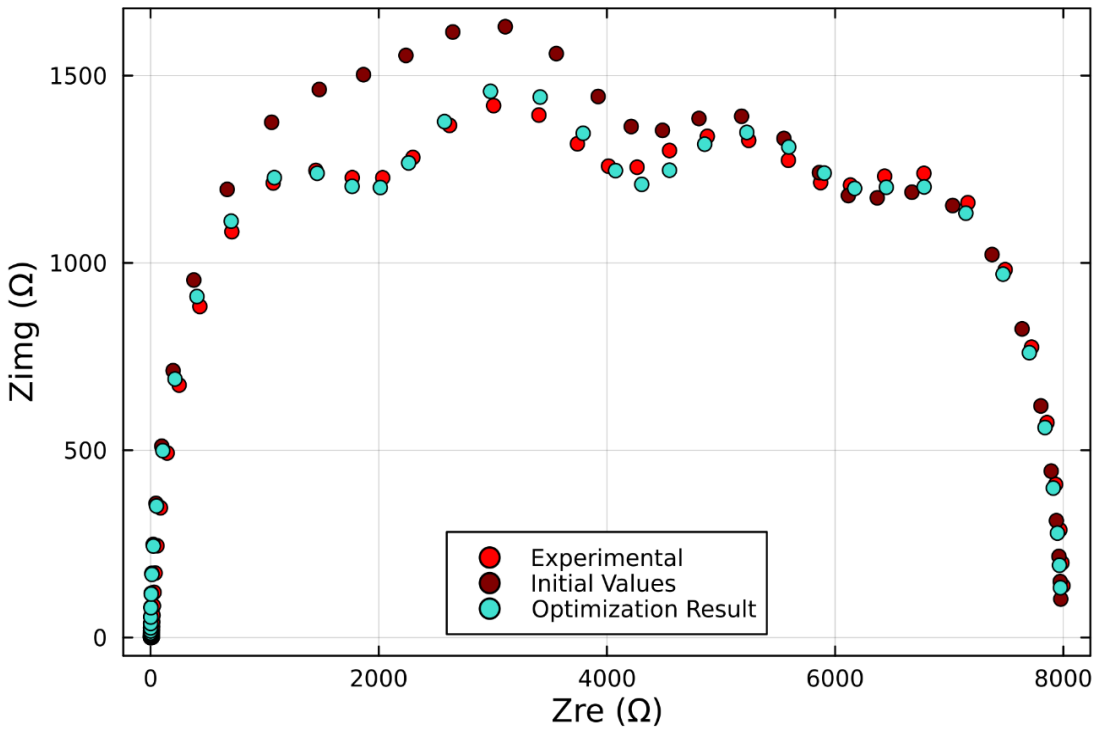

Figure 5. *Theoretical predictions compared with experimental data.*

It is quite apparent that the optimization step was indeed needed to fine tune the discovered parameters. For a better showcasing of the difference in values, table 1 presents the values as they are written on the package by the manufacturer, as measured by me with a multi-meter, the parameter estimation values and the parameter optimization ones.

Circuit Element	Manufacturer	Multimeter	Estimation	Optimization
Rp1 (Ω)	2000	1964	2019.61	2019.61
Rp2 (Ω)	2000	1950	2230.18	2230.18
Rp3 (Ω)	2000	1964	1869.67	1869.67
Rp4 (Ω)	2000	1952	1863.03	1863.03
C1 (μF)	0.47	0.57	0.65	0.42
C2 (μF)	4.7	4.94	3.87	4.42
C3 (μF)	47	47.95	44.09	62.13
C4 (μF)	470	483.4	422.16	543.38

Tabel 1. *Predictions made by parameter estimation algorithm with table of values obtained through different methods underneath*

Now that the program has proven successful in finding parallel RC circuits from the Nyquist plot and discovering an equivalent circuit, I attempted to fit the semicircle section on an actual supercapacitor data (Figure 6 (a)).

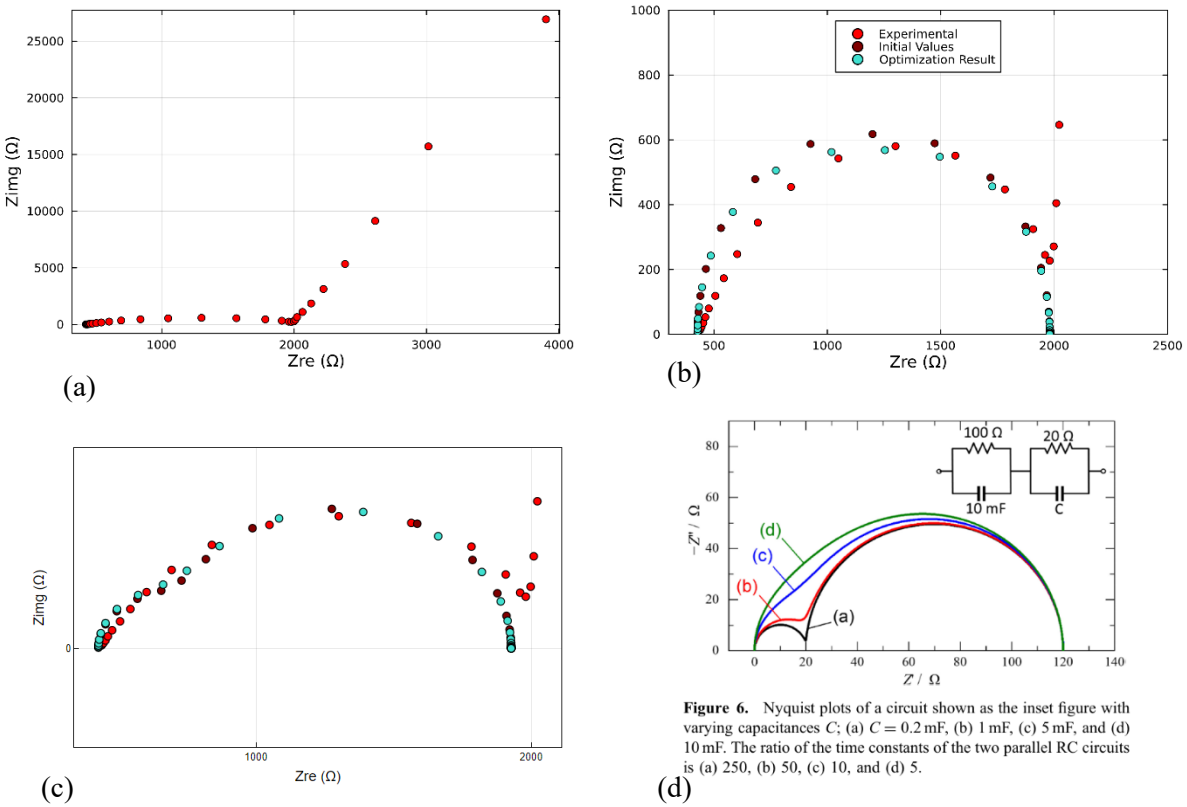

Figure 6. Nyquist plots of a circuit shown as the inset figure with varying capacitances C; (a) $C = 0.2$ mF, (b) 1 mF, (c) 5 mF, and (d) 10 mF. The ratio of the time constants of the two parallel RC circuits is (a) 250, (b) 50, (c) 10, and (d) 5.

Figure 6. *(a) Nyquist plot for a porous Silicon-based supercapacitor. (b) Initial attempt. (c) Second attempt after manually adding another RC circuit. (d) Figure 6 from [10] where the effect of different time constant ratios between two RC circuits are showcased in Nyquist plots*

The semicircle was taken and the program was employed towards finding a model. The first result, Figure 6 (b), looked almost right, but it was clear that something was missing. Because in this case the semicircle had a more irregular, flattened appeareance than the soldered circuit's graph had, it was obvious that probably an additional RC circuit was needed to be added to the model. Unfortunately, the irregular shape also meant they were quite close in time constants, $\tau = RC$, making it increasingly more difficult to determine the parameters of the circuit model for that particular region, as exemplified in Figure 6(d). With this consideration in mind, I was able to manually modify the theoretical model with a second RC circuit whose circuit values I determined in a brute force manner, keeping in mind they had to be quite close to the ones discovered by the program itself (Figure 6 (c)). Now the estimation looked much closer to the original data, but it also made it clear that it is adamant to address this problem going forward.

Chapter 7 Bibliography

1. J. Bezanson, A. Edelman, S. Karpinski, and V. B. Shah, "Julia: A Fresh Approach to Numerical Computing," SIAM Review, vol. 59, no. 1, pp. 65–98, Jan. 2017, doi: 10.1137/141000671
2. T. Breloff, "Plots.jl." Zenodo, Aug. 30, 2023. doi: 10.5281/zenodo.8300728
3. S. Bhagavan, B. de Koning, S. Maddhashiya, and C. Rackauckas, "DataInterpolations.jl: Fast Interpolations of 1D data," Journal of Open Source Software, vol. 9, no. 101, p. 6917, Sep. 2024, doi: 10.21105/joss.06917
4. V. K. Dixit and C. Rackauckas, Optimization.jl: A Unified Optimization Package. (Mar. 15, 2023). Zenodo. doi: 10.5281/zenodo.7738525

5. B. Kamiński et al., JuliaData/DataFrames.jl: v1.5.0. (Feb. 11, 2023). Zenodo. doi: 10.5281/zenodo.7632427
6. J. Quinn et al., JuliaData/CSV.jl: v0.10.11. (Jun. 05, 2023). Zenodo. doi: 10.5281/zenodo.8004128
7. R. A. J. Chagas et al., ronisbr/PrettyTables.jl: v2.3.2. (May 26, 2024). Zenodo. doi: 10.5281/zenodo.11321037
8. J. Heinen et al., jheinen/GR.jl: v0.73.7. (Jul. 22, 2024). Zenodo. doi: 10.5281/zenodo.12794571
9. D. C. Liu and J. Nocedal, “On the limited memory BFGS method for large scale optimization,” Mathematical Programming, vol. 45, no. 1, pp. 503–528, Aug. 1989, doi: 10.1007/BF01589116
10. Kingo ARIYOSHI, Zyun SIROMA, Atsushi MINESHIGE, Mitsuhiro TAKENO, Tomokazu FUKUTSUKA, Takeshi ABE, Satoshi UCHIDA, Electrochemical Impedance Spectroscopy Part 1: Fundamentals, Electrochemistry, 2022, Volume 90, Issue 10

Chapter 8

Systems and Mechanisms Developed for Solving Problems in the Measurement Protocol

8.1 **Encapsulation System for Aqueous/Gel Electrolytes**

The invention relates to a device for encapsulating and forming an electrical contact on each electrode (19) of a parallel-plane supercapacitor device. The device consists of two symmetrical components, each made up of three layers (Figure 1).

The first layer (1), which is in direct contact with the sample, has a central section (2) that facilitates the insertion of the first element of the electrical contact system (9).

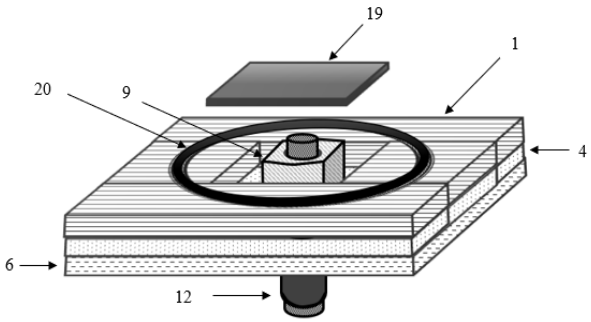

Figure 1. *Assembled encapsulation device component*

The second layer (4) allows the storage of this system between the first layer (1) and the layer to which it will be attached (6). The second element will, in turn, be attached to layer (6), with the side where the electrical contact occurs having a section similar to that on layer (1).

During encapsulation, the sample (19) will be pressed against an elastic force attached to (9), and the electrical contact will be established by pressing the pin from (9) onto the pin from (12). A symmetrical assembly will ultimately be attached to the one described, with a gasket (20) to ensure system insulation, thereby completing the encapsulation.

The invention relates to a device for encapsulation and forming an electrical contact on each electrode (19) of a device parallel plane supercapacitor. The device is consisting of two symmetrical component parts, made up of three layers each.

The first layer, (1), which is in direct contact with the sample has a section in the middle (2) that facilitates insertion of the first element of the contact system electric (9). The second layer, (4) allows storage of this system between the first layer, (1), and the outer layer will be secured (6). The second element will in turn be attached to the layer (6), with the side where the electrical contact will be placed through a section similar to that on layer (1). The sample (19) will be pushed against an elastic force attached to (9), and the contact electrical will be done by pushing the pin in (9) on the pin in (12). A symmetrical assembly it will be followed by the one shown, with a gasket (20) to ensure the isolation of the system and thus encapsulation will be complete.

8.2 **Mechanism for Realizing Contact on the Back of a Supercapacitor**

The invention relates to a connector that can be attached to the back of an electrode to form an electrical contact between the electrode and the external frame (1) of the connector, which can then be connected to an external circuit. This allows the use of the connector in applications where conventional connectors, such as crocodile clips, cannot be used—particularly in electrochemical applications where the electrode surface is immersed in solutions that may be corrosive. This type of connector (Figure 2) allows the complete immersion of the electrode surface in an electrolyte while ensuring the necessary electrical contact to control the potential applied to the electrode (7) during electrochemical processes.

The tube (2), fixed (3) to the connector frame (1), allows the insertion of a screw (6) through a spring

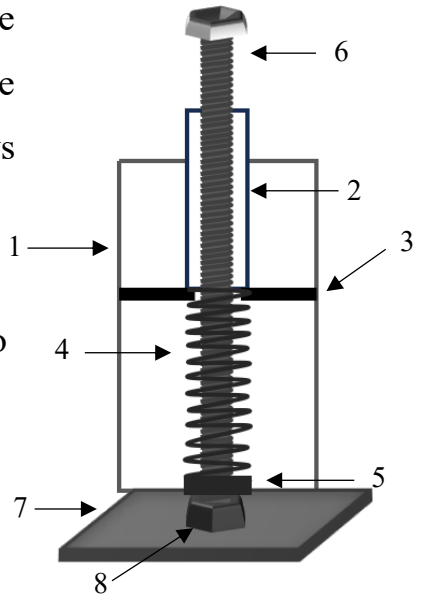

Figure 2. *Cross section view of the connector's mechanism*

(4), which provides an elastic force to pull on the electrode. The nut (5) is partially screwed onto the screw and is intended to secure the screw to the spring, allowing it to deform and reach the nut (8) attached to the electrode (7). When the spring (4) is deformed to the point where the screw (6) makes contact with the nut on the back of the electrode (8), the screw (6) is tightened until it reaches the end of the electrode (7), thereby fixing the screw (6) to the electrode (7).

After fixation, the screw (6) is pulled back, allowing the electrode (7) to come into contact with the connector frame (1). The spring (4), remaining deformed, ensures an elastic force that pulls the electrode (7), keeping it in tight electrical contact with the frame (1). Thus, the formation of the contact on the back of the electrode is complete.

8.3 **Crocodile Connector for Applications Requiring Fine Tuning Operation**

The invention relates to a crocodile connector with an implemented mechanism that allows fine adjustment of the distance between the two ends that will grip the measured electrode. The invention (1) includes a metal frame (2) to which two metal arms (3) are attached, held together by a spring (4) that pulls them together to form an electrical contact between the arms, the electrode (8), and the frame (2).

The screw (7) is threaded into the metal frame (2) to push the slots (5), which, in turn, push the attached arms (3) to raise or lower them depending on how far and in which direction the screw (7) is turned (Figure 3).

The device is a crocodile connector that uses a system to transform rotational motion into vertical motion.

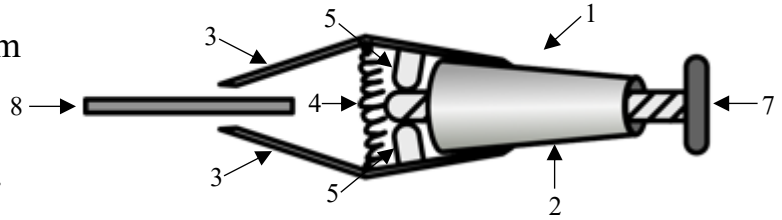

Figure 3. *The presented connector mid clasping a supercapacitor electrode*

Chapter 8 Bibliography

1. Irina-Nicoleta Bratosin, Pericle-Ion Vărășteanu, Dispozitiv pentru încapsularea și realizarea unui contact electric pe un supercapacitor plan paralel, A/00861
2. Irina-Nicoleta Bratosin, Pericle-Ion Vărășteanu, Conector cu prindere de electrozi pentru realizarea unui contact pe spate, A/00278
3. Irina-Nicoleta Bratosin, Pericle-Ion Vărășteanu, Conector crocodil cu sistem de ajustare fina

Chapter 9

Conclusions

The main purpose of this work was to study and improve the electrical performances of Silicon based supercapacitors. In order to obtain a better performance, surface modifications, as well as additional deposition of redox active materials have been performed on the base electrodes, namely heavily p-doped Silicon electrodes. Each stage was studied in detail and measurements were performed towards obtaining a full picture of the feasibility of Silicon supercapacitors as charge storage devices.

Chapter 1 contains a brief preface which presents the main area of interest of this work.

In **Chapter 2** a brief history of the supercapacitor was presented, as well as past and current works and advances made in the supercapacitor field. There is also a section in which this work is placed in the context of the work that came before it and its relevance was emphasized.

In **Chapter 3** a short introduction into the basic theory related to the supercapacitor was presented. The involved measurements, EIS (electrochemical impedance spectroscopy), CV (cyclic voltammetry) and GCD (galvanostatic charge discharge), as well as the physical phenomena involved, electrochemical double layer and pseudocapacitances were described.

Chapter 4 dealt with surface modifications, namely the porosification process of Silicon electrodes. Building on the previously fabricated device, a micro supercapacitor on which molybdenum disulfide nanoflakes and poly-naphthalene methylamine were deposited on its surface, with a PVA-H_2SO_4 solid gel electrolyte (capacitance of 130 mF/cm^3), a similar process was perfected for a large-scale supercapacitor based of porous Silicon electrodes. Two parameters in the porosification process were modified, the exposure time and the applied

current density, and for two electrodes corresponding to one given exposure time and one given current density, electrical measurements were performed for electrical performance assessment, as well as for optimizing the process and picking the most suitable values for further modifications towards performance improvements. On top of the porous Si layer, a conductive polymer, turned carbon composite through thermal treatment was also deposited at the surface to study how an active material would be deposited depending on the degree of porosity and pores length. Since porosity is extensively used in order to increase the surface of a supercapacitor electrode, and, subsequently, its surface capacitance, especially for silicon supercapacitors, having a qualitative, as well as a quantitative description of the porosity's influence was adamant for the progress of silicon- based supercapacitors moving forward. The results of this work were published in the following articles:

Irina-Nicoleta Bratosin, Pericle Varasteanu, Cosmin Romanitan, Alexandru Bujor, Oana Tutunaru, Antonio Radoi, and Mihaela Kusko, In-Depth Analysis of Porous Si Electrodes for Supercapacitors, The Journal of Physical Chemistry C 125 (11), 6043-6054, 2021

Pericle Varasteanu, Cosmin Romanitan, **Irina Bratosin**, Nikolay Djourelov, Raluca Gavrila, Antonio Radoi, Mihaela Kusko, Exploring the impact of MoS_2 on the performance of the planar solid micro-supercapacitor, Materials Chemistry and Physics 265, 124490, 2021

Chapter 5 goes further with the porous Silicon electrode which was determined to give the best charge storage performance in Chapter 4. This time, further enhancements were carried out by growing CoHCF nanocubes on the porous Si's carbonic surface by chronopotentiometry. The resulting electrodes

were assembled in a plane parallel configuration and once again its electrical properties and charge storage performances were assessed through the same type of electrical measurements. While there was a significant improvement in the capacitance value, as well as in energy density, its stability suffered considerably. Therefore, for the next modification, stability was kept at the forefront of the fabrication process. Cobalt hexacyanoferrate has proven itself to be a very promising supercapacitor material, offering a large energy density value, which is one parameter always targeted to be increased for supercapacitors. The results of this work were published in the following article:

Irina-Nicoleta Bratosin, Cosmin Romanitan, Gabriel Craciun, Nikolay Djourelov, Mihaela Kusko, Marius C. Stoian, Antonio Radoi, Graphitized porous silicon decorated with cobalt hexacyanoferrate nanocubes as hybrid electrode for high-performance supercapacitors, Electrochimica Acta 424, 140632, 2022

For **Chapter 6** the strategy was modified. From previous studies it became clear that whatever redox active material was deposited at the surface, no matter how reversible the redox reactions are, there is always a risk of losses and surface passivation through chemical reaction when an electrode is submerged in an electrolyte. With the guarantee of failure, we came prepared. On top of the porous Silicon layer, and on top of the carbon composite presented in Chapter 4, an additional second layer, a TiN layer of 150 nm thickness, was deposited through RF magnetron sputtering. The idea behind this strategy was for the layer underneath, the porous Si layer + carbon composite, to act as a backup layer for the one on top of it, acting as a fail safe for when the first one gives in. At the end of the electrical measurements it was revealed this was exactly what happened,

the TiN layer cracked after 5 000 to 10 000 charging-discharging cycles, revealing the porous layer underneath, which in turn started participating in the charge storage process, extending the overall lifespan of the measured supercapacitor for up to 30 000 charging-discharging cycles, which was an incredible performance compared to previous attempted supercapacitor, as well as for Silicon based supercapacitors in general. The work in this chapter devised a supercapacitor structure which could aid in improving the life cycle of supercapacitors in general, which is an essential goal towards developing more sustainable, long-lasting charge storage devices.

In **Chapter 7**, the process of circuit model discovery was tackled, proposing to use only resistances and capacitances for a circuit simulating the EIS data from a supercapacitor. A circuit made out of commercial resistors and capacitors was assembled in an already known configuration and subjected to EIS measurements, as a supercapacitor would be. A parameter discovery algorithm, where the resistances and capacitances present would be discovered automatically from measured data was programmed in the programming language Julia. After the parameters were determined, they would be input in a second stage of the program where an optimization protocol would use a theoretical model developed using information from the parameter discovery algorithm and would modify the parameters present in said model, resistances and capacitances, in order for the theoretical model to be as close as possible to the measured data. As a result, the program would output the circuit configuration, the corresponding elements and their values, resistances and capacitances. This program was developed from a need to better differentiate between the potential circuit model variants obtained from fitting existing data with a theoretical model, differentiation which is absent from currently available software.

Chapter 8 presents three different patents developed for solving various problems encountered in the measurement process of a supercapacitor. The first patent consists of an encapsulation module meant to preserve the gel electrolyte used and prevent it from drying up/evaporating during prolonged measurements. The second patent is a connector which is meant to be able to ensure a contact made on the back of each constituent electrode of the measured supercapacitor to accommodate a previous encapsulation module, as well as facilitate electro-deposition on the entire surface of a supercapacitor electrode during the electrodeposition process. The third patent is on a crocodile connector with a fine-tuning mechanism. This connector is meant to be used when the current gripping action of the connector is not adequate for the particular application and surface it is supposed to grip.

9.1 Personal Contributions

9.2 Articles:

1. **Irina-Nicoleta Bratosin**, Pericle Varasteanu, Cosmin Romanitan, Alexandru Bujor, Oana Tutunaru, Antonio Radoi, and Mihaela Kusko, In-Depth Analysis of Porous Si Electrodes for Supercapacitors, The Journal of Physical Chemistry C 125 (11), 6043-6054, 2021, **AIS = 0.739**
2. **Irina-Nicoleta Bratosin**, Cosmin Romanitan, Gabriel Craciun, Nikolay Djourelov, Mihaela Kusko, Marius C. Stoian, Antonio Radoi, Graphitized porous silicon decorated with cobalt hexacyanoferrate nanocubes as hybrid electrode for high-performance supercapacitors, Electrochimica Acta 424, 140632, 2022, **AIS = 0.862**
3. Pericle Varasteanu, Cosmin Romanitan, **Irina Bratosin**, Nikolay Djourelov, Raluca Gavrila, Antonio Radoi, Mihaela Kusko, Exploring

the impact of MoS_2 on the performance of the planar solid micro-supercapacitor, Materials Chemistry and Physics 265, 124490, 2021, **AIS = 0.584**

9.3 Patents:

4. **Irina-Nicoleta Bratosin**, Pericle-Ion Vărășteanu, Dispozitiv pentru încapsularea și realizarea unui contact electric pe un supercapacitor plan paralel, A/00861
5. **Irina-Nicoleta Bratosin**, Pericle-Ion Vărășteanu, Conector cu prindere de electrozi pentru realizarea unui contact pe spate, A/00278
6. **Irina-Nicoleta Bratosin**, Pericle-Ion Vărășteanu, Conector crocodil cu sistem de ajustare fina, Pending

9.4 International Conferences:

1. **Irina-Nicoleta Bratosin**, Cosmin Romanitan, Antonio Radoi, Mihaela Kusko, High Performance Quasi-Solid Supercapacitor using Graphitized Porous Silicon Electrodes, 6th International Conference on Advanced Capacitors (ICAC2019), Ueda, Japan, September 8-12, 2019 – oral presentation
2. **Irina-Nicoleta Bratosin**, Cosmin Romanitan, Antonio Radoi, Mihaela Kusko, High Performance Quasi-Solid Supercapacitor using Graphitized Porous Silicon Electrodes, EuroNanoForum 2019 (Nanotechnology and Advanced Materials Progress Under Horizon2020 and Beyond), June 12-14, 2019, Bucharest, Romania – poster
3. **Irina-Nicoleta Bratosin**, Cosmin Romanitan, Antonio Radoi, Mihaela Kusko, In-depth analysis of porous Si electrodes for supercapacitors,

Energy Storage and Conversion, August 4-6, 2021, Virtual Conference – poster

4. **Irina-Nicoleta Bratosin**, Octavian Ionescu, Supercapacitor assembly towards power fluctuations stabilization, 45th International Semiconductors Conference CAS 2022, October 12-14, 2022 Poiana Brasov, Romania – poster
5. **Irina-Nicoleta Bratosin**, Marius C. Stoian, Gabriel Craciun, Nikolay Djurelov, Mihaela Kusko, Antonio Radoi, Improvements on Carbon Based Porous Silicon Supercapacitor Through Electrochemical Deposition of Cobalt Hexacyanoferrate Nanocubes, Smart Materials and Surfaces - SMS 2023 International Conference, 25-27 October 2023 Albufeira/Algarve, Portugal – poster
6. **Irina-Nicoleta Bratosin**, Circuit Model Discovery for Porous Silicon-Based Supercapacitors, JuliaCon, Netherlands, Eindhoven, Philips Stadion, July 9th–13th, 2024 – poster